The Effects of Environmental Wind Shear Direction on Tropical Cyclone Boundary Layer Thermodynamics and Intensity Change from Multiple Observational Datasets

JOSHUA B. WADLER,[a,b] JOSEPH J. CIONE,[a] JUN A. ZHANG,[a,b] EVAN A. KALINA,[c,d] AND JOHN KAPLAN[a]

[a] *NOAA/Atlantic Oceanographic and Meteorological Laboratory/Hurricane Research Division, Miami, Florida*
[b] *Cooperative Institute for Marine and Atmospheric Studies, University of Miami, Miami, Florida*
[c] *Cooperative Institute for Research in Environmental Sciences, University of Colorado Boulder, Boulder, Colorado*
[d] *NOAA/Global Systems Laboratory, Boulder, Colorado*

(Manuscript received 9 February 2021, in final form 4 October 2021)

ABSTRACT: The relationship between deep-layer environmental wind shear direction and tropical cyclone (TC) boundary layer thermodynamic structures is explored in multiple independent databases. Analyses derived from the tropical cyclone buoy database (TCBD) show that when TCs experience northerly component shear, the 10-m equivalent potential temperature θ_e tends to be more symmetric than when shear has a southerly component. The primary asymmetry in θ_e in TCs experiencing southerly component shear is radially outward from 2 times the radius of maximum wind speed, with the left-of-shear quadrants having lower θ_e by 4–6 K than the right-of-shear quadrants. As with the TCBD, an asymmetric distribution of 10-m θ_e for TCs experiencing southerly component shear and a symmetric distribution of 10-m θ_e for TCs experiencing northerly component shear was found using composite observations from dropsondes. These analyses show that differences in the degree of symmetry near the sea surface extend through the depth of the boundary layer. Additionally, mean dropsonde profiles illustrate that TCs experiencing northerly component shear are more potentially unstable between 500- and 1000-m altitude, signaling a more favorable environment for the development of surface-based convection in rainband regions. Analyses from the Statistical Hurricane Intensity Prediction Scheme (SHIPS) database show that subsequent strengthening for TCs in the Atlantic Ocean basin preferentially occurs in northerly component deep-layer environmental wind shear environments whereas subsequent weakening preferentially occurs in southerly component wind shear environments, which further illustrates that the asymmetric distribution of boundary layer thermodynamics is unfavorable for TC intensification. These differences emphasize the impact of deep-layer wind shear direction on TC intensity changes that likely result from the superposition of large-scale advection with the shear-relative asymmetries in TC structure.

SIGNIFICANCE STATEMENT: This research investigates how the direction of the winds surrounding the storm impacts the strength of a tropical cyclone. Analyses from this study illustrate that when the winds come from the south the atmospheric boundary layer has a cool and dry side along with a warm and moist side. When the large-scale winds come from the north, temperature and moisture conditions are more uniform throughout the boundary layer. Consequently, results from tropical cyclone climatology show that winds observed to come from the north favor subsequent intensification. These relationships illustrate that tropical cyclone structure and intensity are directly influenced by their surrounding environments and that knowledge of the wind environment could help to improve future forecasts of tropical cyclone intensity change.

KEYWORDS: Wind shear; Boundary layer; Synoptic-scale processes; Tropical cyclones; Thermodynamics

1. Introduction

Landfalling tropical cyclones (TCs) cause devastating loss of life and billions of dollars annually in property damage (e.g., Pielke and Landsea 1998; Pielke et al. 2008; Klotzbach et al. 2018). While track forecasts have significantly improved over recent years, providing coastal communities additional lead time to prepare, the accurate prediction of TC intensity changes remains a challenge to both the operational and research communities due to the multiscale interactions that control storm evolution (e.g., Marks and Shay 1998; Rogers et al. 2006, 2013a; DeMaria et al. 2014).

In recent years, many studies have shown that TC intensity changes are related to how a storm responds to deep-layer environmental vertical wind shear, defined as the difference in environmental winds between 850 and 200 hPa (hereinafter referred to as shear). Generally, these studies show that a critical factor controlling whether the TC undergoes intensification is its resilience to both kinematic and thermodynamic asymmetries resulting from shear. For example, Rogers et al. (2013b) used an airborne radar database to show that the distribution of convection is more symmetric in intensifying storms when compared with steady-state systems, which have a greater concentration of convection in downshear quadrants. The linkage between convection propagating into the upshear-left (USL) quadrant and subsequent intensification is confirmed in several observational (e.g., Stevenson et al. 2014, 2018; Zagrodnik and Jiang 2014; Alvey et al. 2015; Rogers et al. 2015, 2016; Rios-Berrios and Torn 2017; Wadler et al. 2018a) and modeling studies (e.g., Chen and Gopalakrishnan 2015; Onderlinde and Nolan 2014, 2016; Rios-Berrios et al. 2016a,b; Leighton et al. 2018; Zhang and

Corresponding author: Joshua B. Wadler, joshua.wadler@noaa.gov

DOI: 10.1175/MWR-D-21-0022.1

Rogers 2019). Satellite-based studies also highlight the importance of storm symmetry for intensification, and generally emphasize the importance of stratiform precipitation and shallow convection (e.g., Jiang 2012; Kieper and Jiang 2012; Zagrodnik and Jiang 2014; Tao and Jiang 2015; Tao et al. 2017). Using satellite composites, Jiang et al. (2018) found that an increase in stratiform precipitation occurs ~18 h before the onset of rapid intensification [RI; a greater than 30-kt (1 kt ≈ 0.51 m s^{-1}) increase in intensity over 24 h] and that an increase in shallow convection occurs ~3 h before the onset of RI.

It is likely that convective and precipitation symmetry for TCs in shear is related to the midlevel and boundary layer thermodynamic profiles. Alvey et al. (2020) showed that ensemble simulations of Hurricane Edouard (2014) favored RI when specific humidity values were increased upshear. This finding supports results from recent observational case studies by Zawislak et al. (2016) and Nguyen et al. (2017), who showed that persistent precipitation propagation into the upshear quadrants did not occur until increased midlevel relative humidity (RH) values were observed. Alvey et al. (2020) found that the increased upshear midlevel humidification was the result of the evaporation and sublimation of condensate from downshear deep convection being advected upshear.

One process that can reduce thermodynamic symmetry is ventilation, that is, the mixing of dry environmental air into the TC circulation. Previous studies have defined ventilation through low-level (e.g., Riemer et al. 2010) and midlevel (e.g., Tang and Emanuel 2010, 2012) processes. More generally, Alland et al. (2021a,b) defined ventilation through two distinct pathways: radial and downdraft. Through radial ventilation, the dry air can directly reduce midlevel humidity and mix with the eyewall (Tang and Emanuel 2010, 2012; Alland et al. 2017, 2021a). In downdraft ventilation, the low-θ_e air can be transported into the boundary layer through downdrafts underneath quasi-persistent convection typically in the left-of-shear quadrants (Riemer et al. 2010, 2013). In the simulations by Riemer et al. (2010), the amount of low-θ_e air transported into the boundary layer via convective downdrafts is amplified with increasing shear magnitude.

While the Riemer et al. (2010) simulations showed low-θ_e air from downdrafts entering the eyewall, which effectively reduced the efficiency of the TC heat engine, observational case studies (Molinari et al. 2013; Zhang et al. 2017; Wadler et al. 2018b; Rudzin et al. 2020), dropsonde composite studies (Zhang et al. 2013, Nguyen et al. 2019), and modeling studies (Alland et al. 2021a; Chen et al. 2021) illustrate that as parcels travel from the downdraft region to the downshear-right (DSR) quadrant, which is the primary region for convective initiation (Reasor et al. 2013; DeHart et al. 2014) due to the convergence of low-level vorticity in an area of high θ_e (Riemer 2016), the air-sea enthalpy fluxes can provide enough energy to recover the low-θ_e air in parcels to values that existed in the DSR quadrant prior to the downdrafts occurrence. Since high-θ_e air entering the eyewall is favorable for convective development, the amount of air–sea enthalpy fluxes downwind of convective downdrafts in the left-of-shear quadrants is likely linked to future TC intensification. For example, in a composite study by Cione et al. (2013), intensifying storms were shown to have a statistically significant larger air-sea moisture contrast downshear and right-of-shear (signaling larger moisture fluxes, assuming no difference in wind speed distribution) relative to weakening systems. Besides larger near-surface wind speeds, locally enhanced air–sea enthalpy fluxes can result from limited low-level atmospheric moisture (Cione 2015) or high sea surface temperatures (SSTs; e.g., Shay et al. 2000; Jaimes and Shay 2015, 2016; Wadler et al. 2021a).

The above discussion highlights how structural asymmetries in TCs due to shear are related to intensity change. However, the deep-layer vertical wind shear is a simple vector difference of large-scale averaged winds at two pressure levels. Properties of the environmental wind profile are also important for TC development and formation. For example, Finocchio et al. (2016) showed that the vertical structure of the environmental wind profile (i.e., low-level shear or upper-level shear, regardless of the shear direction) influences TC development, with shallow and low-level shear being the most destructive for TCs. The orientation of the environmental low-level wind field relative to the shear also plays an important role in a TC's intensity evolution (Rappin and Nolan 2012; Chen et al. 2018, 2019). The simulations by Rappin and Nolan (2012) showed that enhanced surface fluxes left-of-shear favored TC intensification when the low-level mean flow was oriented opposite of the shear vector. Chen et al. (2018) showed that when the low-level mean flow is oriented toward the left-of-shear direction, there were enhanced storm-relative wind speeds (and air–sea enthalpy fluxes) through inflow trajectories in the downshear quadrants, promoting convective symmetry that is efficient for intensification (e.g., Nolan and Grasso 2003; Nolan et al. 2007). Tropical cyclone-relative environmental helicity (TCREH) is also related to storm symmetry, as positive TCREH promotes eyewall convective symmetry and rapid recovery of low-θ_e air in the boundary layer resulting from downdrafts (Onderlinde and Nolan 2014, 2016).

The horizontal direction of the deep-layer wind shear vector has also been linked to TC genesis and storm structure. For genesis, easterly shear is statistically more favorable than westerly shear (Tuleya and Kurihara 1981), but that may be due to easterly shear occurring in more favorable environmental thermodynamic conditions (Nolan and McGauley 2012). For developed storms, Cione et al. (2013) highlighted that TCs experiencing southerly shear had higher atmospheric specific humidity values downshear and right-of-shear, but TCs experiencing northerly shear had more symmetric moisture distributions. What has not been studied is how the horizontal direction of the deep-layer wind shear vector impacts Atlantic basin TC intensity change through its impact on the degree of asymmetry in both boundary layer thermodynamic and kinematic characteristics, the primary objective of this paper. The specific goals are to

1) diagnose how shear direction is climatologically correlated to Atlantic basin TC intensity changes,
2) characterize how the near-surface thermodynamic distributions and boundary layer stability profiles are linked to shear direction, and
3) tie the results of goal 2 to TC intensity change and provide physical reasoning for how the shear direction affects the near-surface thermodynamics due to the combined effect of environmental gradients and the shear-induced asymmetry.

2. Data and method

a. Tropical cyclone buoy database

The primary analysis tool for studying the distribution of thermodynamic structures in relation to environmental wind shear is the tropical cyclone buoy database (TCBD) that contains post-processed and quality-controlled near-surface in situ measurements from the National Data Buoy Center (NDBC; Gilhousen 1988, 1998) and Coastal-Marine Automated Network (C-MAN) platforms [see Cione et al. (2000) for details about the quality control]. The buoys directly measure sea surface temperature (SST) and atmospheric temperature, humidity, pressure, and wind speed from fixed-length platforms near the sea surface and have been used to study a variety of air–sea interaction processes in the hurricane environment (Cione et al. 2000, 2013; Cione and Uhlhorn 2003; Cione 2015). In this study, the collocated in situ atmospheric and oceanic measurements from the buoys are used to calculate sensible heat and latent heat fluxes [Eqs. (1) and (2), respectively; combined, they are referred to as enthalpy flux]:

$$Q_s = \rho_a c_p C_h U_{10}(\mathrm{SST} - T_{10}) \text{ and} \tag{1}$$

$$Q_l = \rho_a L_v C_e U_{10}(q_s - q_{10}), \tag{2}$$

where ρ_a is the density of dry air, $C_h = C_e = 1.1 \times 10^{-3}$ are the exchange coefficients for sensible heat and latent heat fluxes, respectively [values derived from Zhang et al. (2008)], $c_p = 1004$ J kg^{-1} K^{-1} is the specific heat of dry air at constant pressure, $L_v = 2.5 \times 10^6$ J kg^{-1} is the latent heat of evaporation, U_{10} is the 10-m wind speed, T_{10} and SST are the 10-m air and sea surface temperature, respectively; and q_{10} and q_s are the 10-m and sea surface specific humidity, respectively.

A unique aspect of this measurement platform is obtaining observations farther from the TC center than standard aircraft-based measurements (e.g., dual-Doppler radar and dropsondes), which are often limited to within 200–250 km from the TC center, allowing for an analysis of how the TC interacts with its nearby synoptic environment. With buoys fixed in space and reporting measurements hourly (using observations between minutes 52–60), they have the ability to measure Eulerian time series as TCs move through the basin. To ensure the observations in this research have tropical characteristics, the TCBD observations had to be within 555 km of a TC center, south of 35° latitude, and exhibit SSTs greater than 26°C. In this study, tropical depressions were excluded so as to only include storms with organized circulations. In addition, TCs that made landfall within 12 h of the observations were discounted due to the effect of land interactions on the TC circulation and thermodynamic distribution. Currently, the TCBD includes data for storm events that occurred between 1978 and 2017.

All buoy locations and time series used in this study from the updated database are given in Fig. 1. With the constraints described above applied to the updated database, there are a total of 274 buoys that are primarily located throughout the Gulf of Mexico and near the east coast of the United States (Fig. 1a). Additional platforms are located near the Bahamas and in the Caribbean Sea. In total, there are 2393 time series that span the entire western Atlantic TC basin (Fig. 1b), although they are biased toward nearshore regions and north of 20°N. Of those time series, 1806 are for tropical storms, 380 are for minimal hurricanes (category 1–2 on the Saffir–Simpson scale), and 207 are major hurricanes (category 3–5 on the Saffir–Simpson scale).

In addition to in situ measurements, each TCBD observation is matched with environmental diagnostics from the Statistical Hurricane Intensity Prediction Scheme (SHIPS) database, including environmental variables, such as the 850–200-hPa environmental wind shear vector computed from Global Forecast System (GFS) analyses (see section 2c for further details). These measurements are also linked with data associated with the corresponding TC, including its location, maximum sustained 10-m wind speed, and minimum central pressure from the Atlantic hurricane (HURDAT2; Landsea and Franklin 2013) database, as well as estimates of the radius of maximum wind speed (RMW) from the extended best track (EBT; Demuth et al. 2006) database. The variables from those databases are linearly interpolated between points that are 6 h apart to the time of the buoy observation.

The RMW from the EBT is utilized so that composites derived from the TCBD can be normalized relative to the RMW. The normalized radius r^*, where r^* = radius/RMW, coordinate system is commonly utilized in observational composites (e.g., Rogers et al. 2013b; Reasor et al. 2013; Cione et al. 2013; Zhang et al. 2013) because it allows for an analysis of how the distributions relate to the known storm structure. Of note, the RMW in the EBT has known limitations and uncertainties such as instances where the EBT-reported RMW is larger than one or more of the (34, 50, or 64 kt) wind radii (Landsea and Franklin 2013; Davis 2018). In Davis (2018), there was often significant disagreement between the objectively calculated and EBT-reported RMW, even in major hurricanes that typically have well-defined RMW values. In this study, efforts were made to eliminate unrealistic values of the RMW, and the analyses derived from the TCBD were also computed using physical, non-normalized, coordinates for further verification of the results. The comparison between the normalized and physical coordinates is discussed throughout the present study.

b. Dropsondes

In addition to measurements from the TCBD, this study utilizes measurements derived from dropsondes, which are commonly released on aircraft reconnaissance and research missions. Dropsondes measure single profiles of wind speed, wind direction, temperature, and humidity with an ~7-m vertical resolution (Hock and Franklin 1999). With the TCBD observations only being near-surface, dropsonde observations provide the ability to study a deeper layer of the atmosphere (typically up to 3000 m, the altitude of NOAA P-3 during in-storm missions), and to independently corroborate patterns noticed from the TCBD derived analyses.

Each dropsonde is postprocessed with NCAR's Atmospheric Processing Environment (Aspen) software and put into storm-centered coordinates using storm centers determined by the 2-min resolution track data (available at https://www.aoml.noaa.gov/hrd/Storm_pages) based on aircraft fixes following the method of

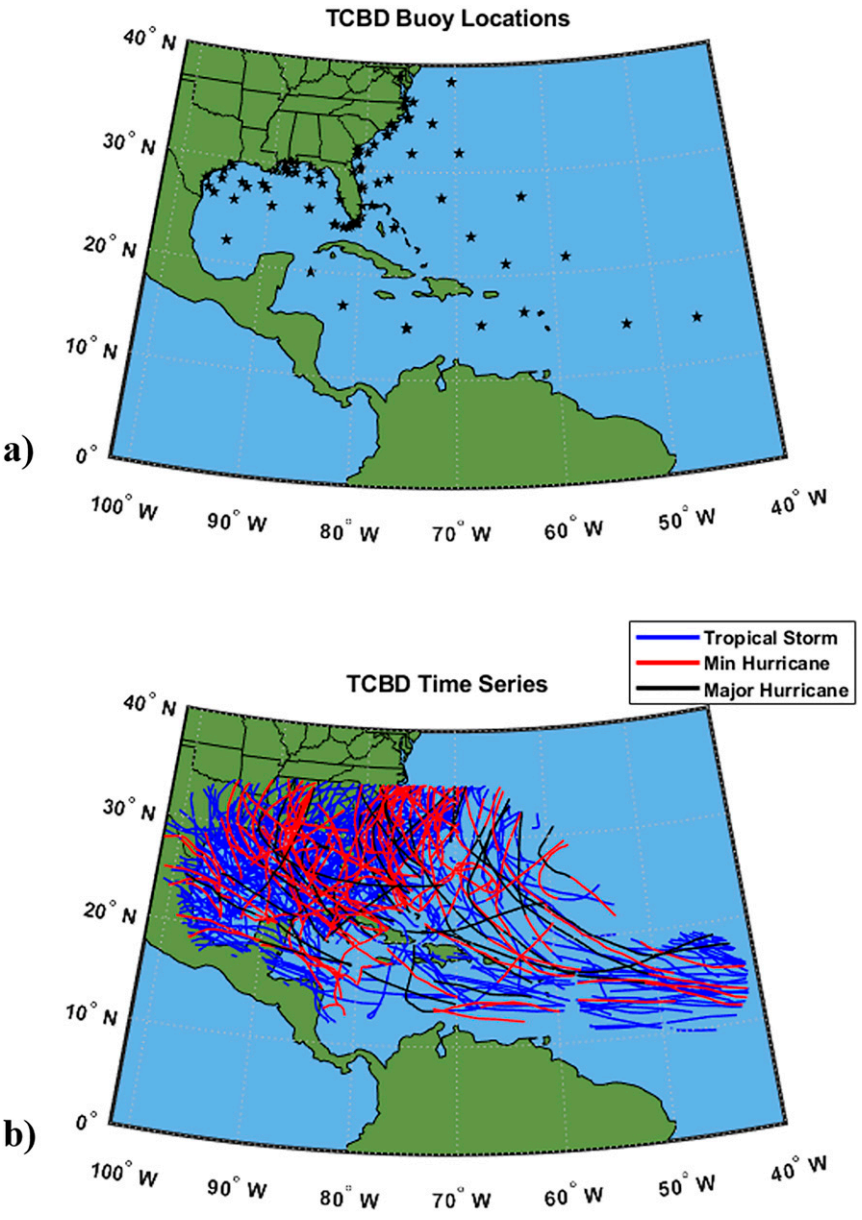

FIG. 1. A geographical map of (a) buoy locations (black stars) and (b) storm tracks from the TCBD that were used in this study. In (b), the tracks are color coded on the basis of maximum TC intensity.

Willoughby and Chelmow (1982). In this study, we analyze dropsonde data in TCs from 1999 to 2014 that were collected by NOAA WP-3D (P-3) and G-IV, Air Force C-130, and NASA DC-8 aircraft and Global Hawk. This dataset is an extension of that given by Zhang et al. (2013, 2020). For the purpose of investigating the boundary layer and near-surface structures, only dropsondes that have wind, temperature and humidity observations below 50-m altitude are included in the analysis. Additionally, we only used profiles that contain less than a 50-m vertical gap at any point within the dropsonde profile. A total of 3612 quality-controlled dropsondes are included in the composite analysis, of which 304 are from tropical storms, 1427 are from minimal hurricanes, and 1881 are from major hurricanes.

As with the analyses derived from the TCBD, the dropsonde data are composited as a function of radius that is also normalized relative to the RMW, which was determined from the maximum surface wind speed measurements from the stepped frequency microwave radiometer (SFMR; Uhlhorn et al. 2007; Klotz and Uhlhorn 2014). The storm-relative locations of the dropsonde observations at 10-m altitude are in Fig. 2. While most of the measurements are close to the inner core (67% of observations within $r^* = 2$), observations extend outward to the synoptic environment surrounding the storm. Of note, the RMW

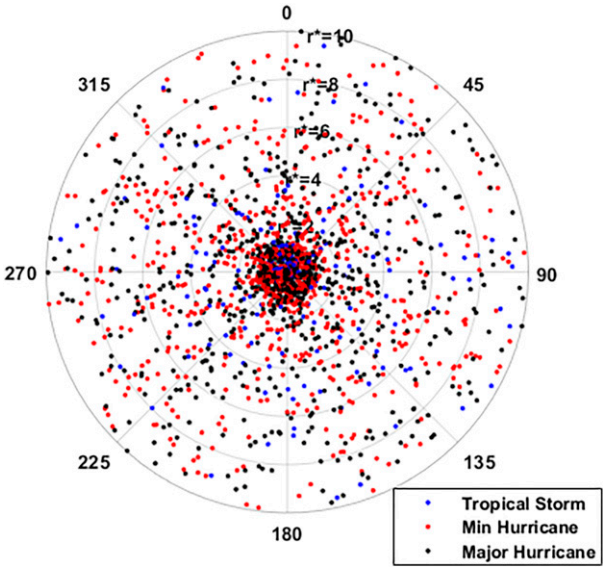

FIG. 2. The distribution of dropsonde locations at 10-m altitude in normalized radial r^* (r^* = radius/radius of maximum wind speed), and azimuthal coordinates. The observations are color coded on the basis of TC intensity.

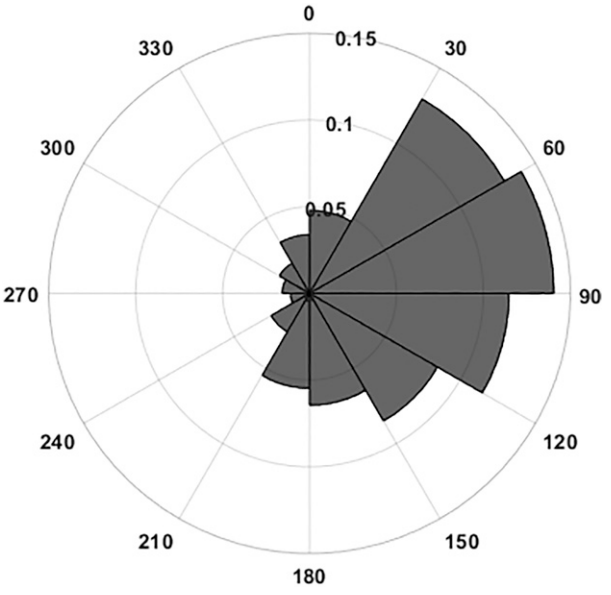

FIG. 3. The normalized distribution (normalized by total number of cases) of all shear headings in the TCBD.

measurements likely have a small low bias as compared with the more commonly used 2-km-altitude RMW from aircraft Doppler radar measurements (e.g., Rogers et al. 2013b, 2015, 2016; Reasor et al. 2013; Wadler et al. 2018a,b, 2021a) because of the outward slope with height of the hurricane eyewall and its associated wind field (e.g., Stern and Nolan 2009; Rogers et al. 2012; Hazelton et al. 2015). However, given that the sample size of the SFMR derived RMW is much larger than that of radar derived RMW (Air Force flights only have SFMR data), and that our research focuses on surface-based air–sea interaction processes, the surface RMW is used in the composite analysis.

c. *Statistical Hurricane Intensity Prediction Scheme*

The Statistical Hurricane Intensity Prediction Scheme (SHIPS) is a multiple-linear regression model that provides operational intensity forecasts every 6 h for tropical and subtropical cyclones in both the Atlantic and eastern North Pacific basins (DeMaria et al. 2005). The SHIPS model is rederived prior to each hurricane season utilizing a developmental database that includes atmospheric, oceanic, and satellite derived predictors for all tropical and subtropical cyclones that formed between 1982 and the present. The atmospheric predictors included in the SHIPS database are derived from the National Centers for Environmental Prediction (NCEP) 1° × 1° latitude–longitude resolution Climate Forecast System Reanalyses (Saha et al. 2010) between 1982 and 1999 and Global Forecast System (GFS) operational analyses of that same resolution from 2000 to the present. The SHIPS database also includes satellite predictors derived from Geostationary Operational Environmental Satellites (GOES) infrared imagery (Mueller et al. 2006) and oceanic predictors derived from both the Reynolds (Reynolds and Smith 1993) and Navy Coupled Ocean Data Assimilation (NCODA; NCODA 2019) ocean analyses.

In this study, several predictors from the SHIPS developmental database were explicitly examined for every TC of tropical storm strength or greater in the Atlantic basin between 1982 and 2017 (i.e., not only the TCs in the TCBD and dropsonde databases). Those predictors (acronyms in parenthesis are the variable names in the SHIPS database) include the magnitude (SHRD) and heading (SHTD) of the deep-layer vertical shear of the horizontal wind, the shallow-layer vertical shear (SHRS) and direction (SHTS), the near-surface equivalent potential temperature (E000), the low-level (RHLO), midlevel (RHMD), and upper-level (RHHI) relative humidity and the sea surface temperature (RSST) beneath the storm. The magnitude and heading of the vertical shear of the horizontal wind between 200 and 850 hPa are determined by subtracting the 200–800-km radius area-averaged u and v components of the wind at 200 hPa from those at 850 hPa. The RHLO, RHMD, and RHHI predictors are the 200–800-km area-averaged and mass-weighted relative humidity within the 850–700-, 700–500-, and 500–300-hPa layers, respectively. E000 is computed utilizing the 200–800-km area-averaged temperature and moisture values at the 1000-hPa level. Last, sea surface temperature at the storm center (RSST) is estimated by linearly interpolating the weekly 1° × 1° latitude–longitude Reynolds (Reynolds and Smith 1993) sea surface temperatures obtained from the last available analysis prior to storm arrival. Note that all of the above SHIPS variables are evaluated utilizing the storm location and intensity information contained in the HURDAT2 dataset.

3. Results

a. *TCBD thermodynamic composite analyses*

The normalized distribution of all deep-layer (850–200 hPa) environmental wind shear headings for TCs in the

TABLE 1. A comparison of environmental variables in the TCBD for TCs experiencing northerly component and southerly component shear. All of the differences are statistically significant at 99% confidence interval except the 850–200-hPa shear magnitude.

	TCs experiencing northerly component shear	TCs experiencing southerly component shear
850–200-hPa shear magnitude (kt)	14.5	14.6
850–500-hPa shear magnitude (kt)	6.1	6.9
850–700-hPa, 200–500-km area-averaged relative humidity (%)	67.1	68.3
700–500-hPa, 200–500-km area-averaged relative humidity (%)	56.5	56.8
Sea surface temperature (°C)	28.6	28.4
Latitude (°)	25.9	25.7
Longitude (°)	−76.1	−77.9
Initial intensity (kt)	63.2	70.5

TCBD is given in Fig. 3. The most common shear headings are between 30° and 120° and the large majority (78.5%) of TCs in the database experience westerly shear. To diagnose how shear direction impacts the thermodynamic distributions, the TCBD time series are subdivided into cases when the shear has a northerly component (i.e., shear pointing to the south; heading between 90.1° and 269.9°) and southerly component (i.e., shear pointing to the north; heading between 270.1° and 89.9°). The two groups are large with 17 629 distinct buoy measurements from TCs experiencing northerly component shear and 16 916 buoy measurements from TCs experiencing distinct southerly component, and they are chosen because both shear components are commonly observed. Note that we did not compare easterly versus westerly shear cases, such as was done in the genesis studies of Tuleya and Kurihara (1981) and Nolan and McGauley (2012), because easterly shear is relatively rare. While the northerly component shear cases have slightly more favorable environmental conditions for TC development (Table 1), the two groups experience comparable mean initial shear magnitudes between 850 and 200 hPa and between 850 and 500 hPa, SSTs, 850–700- and 700–500-hPa relative humidity values, and latitudes. The similar environmental conditions control for differences between the groups being attributed to different environmental regimes. The differences in mean longitude (i.e., southerly component shear TCs being farther west) is due to a higher concentration of TCs in the northern Gulf of Mexico in southerly component shear cases (not shown). The initial mean intensity of 63.2 and 70.5 kt is also comparable between TCs experiencing northerly component and southerly component shear, respectively.

Each TCBD observation is further stratified into a shear-relative quadrant and put into normalized radial bins (bin spacing is one RMW). Outside of the innermost radial bin, each radial bin of each quadrant has more than 100 unique observations (with a mean of 245 observations in each radial bin/quadrant; not shown). Radially outward of $r^* = 2$, the near-surface θ_e in the southerly component shear cases is more asymmetric than in the northerly component shear cases (Fig. 4). Between $r^* = 2$ and $r^* = 10$ of the southerly component shear cases (Fig. 4a), the USL and downshear-left (DSL) quadrants generally have mean θ_e values between 352 and 355 K while the upshear-right (USR) and DSR quadrants have values between 356 and 359 K. In every radial bin between $r^* = 2$ and $r^* = 10$, the differences between the left-of-shear and right-of-shear quadrants are statistically significant for at least the 95% confidence interval (as indicated by no overlap of the shaded error bars).

In contrast to TCs experiencing southerly component shear, there is no clear θ_e asymmetry between the quadrants in the

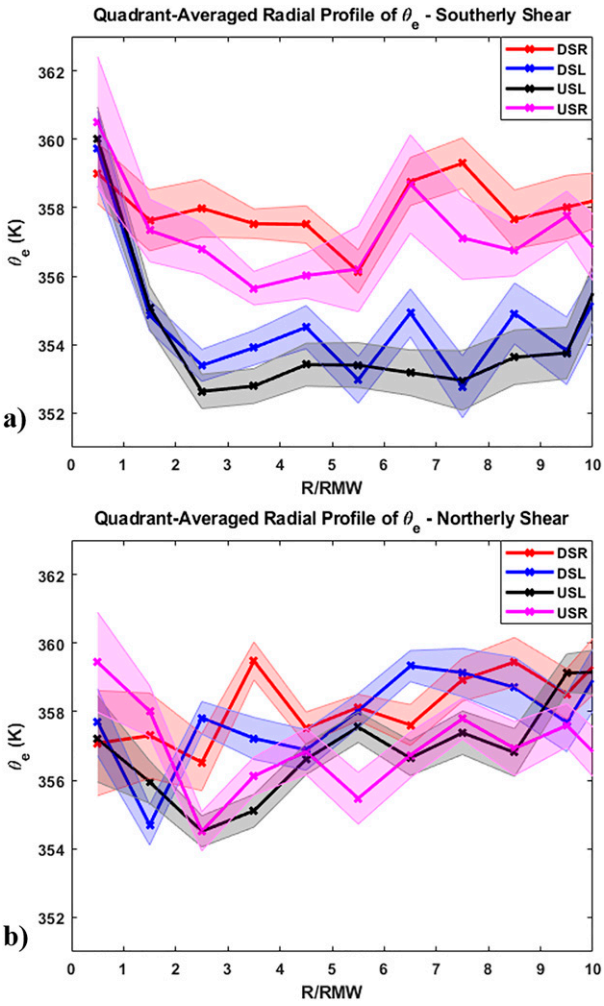

FIG. 4. Radial profiles of quadrant-averaged equivalent potential temperature θ_e near the sea surface for TCs experiencing (a) southerly component shear and (b) northerly component shear. In both panels, the quadrant averaging is relative to the deep-layer environmental wind shear with the downshear-right (DSR), downshear-left (DSL), upshear-left (USL), and upshear-right (USR) quadrants outlined. Radial binning is by 1 times the radius of maximum wind speed (RMW). Shading for each line is 2 times the standard error in each direction.

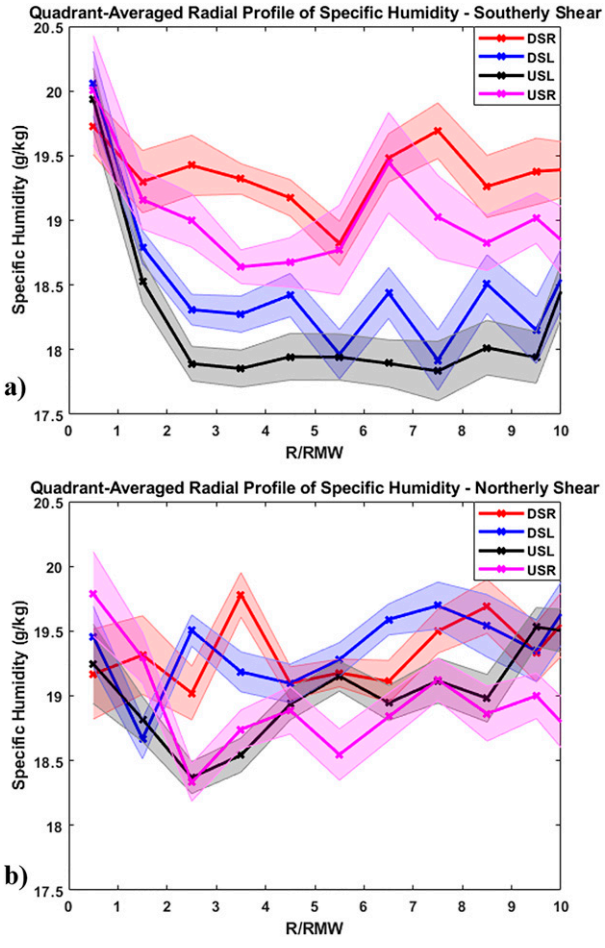

FIG. 5. As in Fig. 4, but for atmospheric specific humidity q_a.

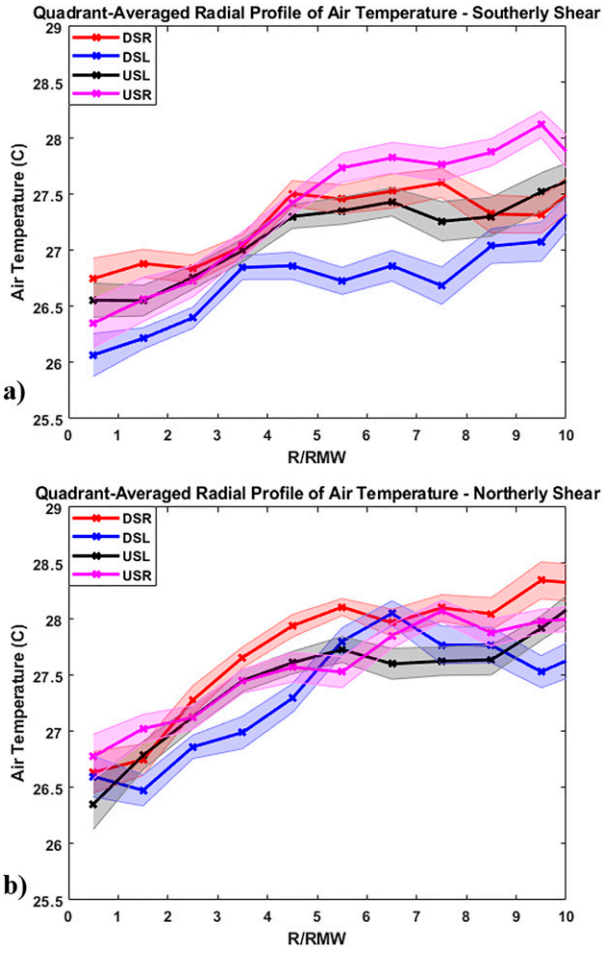

FIG. 6. As in Fig. 4, but for atmospheric temperature T_a.

northerly component shear cases (Fig. 4b). The differences between the quadrants are not statistically significant in the northerly component shear cases at most r^*, with θ_e values radially outward of $r^* = 2$ generally ranging between 355 and 359 K and a mean close to 357 K in all radial bins. Note that the patterns depicted in Fig. 4 are nearly identical when there is a buffer zone between the groups such that the northerly component shear heading is between 100° and 260° and the southerly component shear heading is between 280° and 80° (not shown).

The atmospheric specific humidity q_a fields show a similar distribution to θ_e (Fig. 5). In the southerly component shear cases (Fig. 5a), q_a is significantly lower in the left-of-shear quadrants than in the right-of-shear quadrants. The lowest mean q_a values are ~17.8 g kg^{-1} (USL quadrant) while the largest mean q_a values, typically in the DSR quadrant, are ~19.5 g kg^{-1}. Since the latent heat flux may not always be sufficient to supply the additional energy transfer needed for θ_e values to recover by the time parcels reach the DSR quadrant (i.e., the typical region of convective development), the moisture asymmetry presents an unfavorable thermodynamic distribution for the development of convection and subsequent storm intensification (discussed further below). In contrast, the northerly component shear cases generally have no distinct asymmetry with quadrant-averaged q_a values between 18.5 and 19.5 g kg^{-1} (Fig. 5b), although the upshear quadrants generally have lower q_a values than the downshear quadrants. The symmetric distribution of atmospheric moisture limits the necessity for the boundary layer θ_e values to recover between the typical region of convective downdrafts (DSL and USL quadrants) and the typical region of convective development (DSR quadrant).

The atmospheric temperature T_a fields show a slightly different distribution than θ_e and q_a (Fig. 6). Throughout all radial bands, neither the southerly component shear nor northerly component shear cases exhibit a wavenumber-1 asymmetry. However, in the southerly component shear cases (Fig. 6a), the DSL quadrant has statistically significant cooler temperatures than the other quadrants by ~0.75°–1°C, which all have similar T_a values between $r^* = 3$ and $r^* = 6$. While T_a values generally increases with increasing radius, in the DSL quadrant it ranges between 26.5° and 27°C from $r^* = 3$ to $r^* = 8$. At these radii, T_a values are greater than 27°C in the other quadrants. The lower T_a values in the DSL quadrant may be due to a combination of convective downdrafts in the outer-core region and large-scale transport of cooler air on the northern side of TCs (discussed further below). In

the northerly component shear cases (Fig. 6b) the DSL quadrant is also cooler than the others between $r^* = 2$ and $r^* = 5$ by a statistically significant margin, but the reduction is only ~0.25–0.5°C. The reduced cooling is likely because the DSL quadrant is typically on the eastern side of TCs experiencing northerly component shear (i.e., in an area characterized by advection of warm/moist air, discussed further below).

The differences in the distribution of near-surface thermodynamics between the two shear direction groups have significant implications for subsequent TC intensity change. In nonnormalized plan view (Figs. 7a,b) using a bin spacing of 100 km (data distribution in Figs. 7d,e), the highest θ_e values for both shear direction groups are in the southeastern quadrant. With a median shear heading of 51° for southerly component shear cases, the right-of-shear quadrants[1] (i.e., southeast area of a storm) are characterized by θ_e values exceeding 357 K, while the left-of-shear quadrants are characterized by θ_e values below 354 K. This wavenumber-1 asymmetry (which exists both inside and outside the inner-core region) in near-surface θ_e is similar to that presented in the simulations of Riemer et al. (2010) and in observational composites (e.g., Zhang et al. 2013). However, we note that the differences between the quadrants cannot be solely attributed to downdraft ventilation (and thus vortex tilt) since convective downdrafts are concentrated in rainband regions that are typically near $r^* = 2$ and $r^* = 3$ (~100–200-km radius; e.g., Willoughby et al. 1984; Wang 2009; Riemer et al. 2010).

In contrast to southerly component shear cases, TCs experiencing northerly component shear (with a mean shear heading of 147°; Fig. 7b) have a less-amplified 10-m θ_e asymmetry (data distribution in Fig. 7e), although the values outside the inner-core are still largest in the southeast (DSR) quadrant. Using a Student's t test that assumes unequal variances, significant differences (at 95%) between the groups are noted outside the inner-core in every quadrant (Fig. 7c). The largest differences are in the northwest quadrant, with the higher values from TCs experiencing northerly component shear by 4–6 K. In a normalized shear-relative framework, the largest θ_e differences are in the left-of-shear quadrants (similar result to Fig. 4, not shown), with the TCs experiencing northerly component shear also having higher values by 4–6 K.

As stated earlier, since the thermodynamic differences are continuously statistically significant between $r^* = 2$ and $r^* = 10$ and are not in the same shear-relative locations, they cannot be solely attributed to convective downdrafts. With the buoy data biased toward nearshore regions and north of 20°N, we hypothesize that the superposition between the location of convective downdrafts with large-scale horizontal advection is responsible for the different thermodynamic distributions. In both shear direction groups, there is negative horizontal θ_e advection on the west and southwestern sides of the TCs (i.e., equatorward advection of subtropical low-θ_e air; Fig. 8). With the negative θ_e advection occurring on the western side of the TCs (and different shear-relative locations) for both shear direction groups, it is most likely a combination of being from the environment and from vortex-scale transport of air from downdraft ventilation. The negative advection has a larger magnitude in the southerly component shear cases (Fig. 8a, maximized at ~ -1.5 K h^{-1}), and occurs in the USR quadrant, which likely counteracts boundary layer recovery in this region (discussed further below). With a θ_e maximum in the southeastern quadrant of both shear direction groups, each has positive θ_e advection on the eastern side of the storms (i.e., poleward advection of high-θ_e tropical air). The positive horizontal θ_e advection is of a larger magnitude in the northerly component shear cases (Fig. 8b, maximized at ~1.5 K h^{-1}), and is located in the DSL quadrant, which can help to partially offset the negative effects of downdrafts typical of this region (e.g., Riemer et al. 2010). The θ_e advection in the southerly component shear cases becomes positive in the DSR quadrant, which may lead to insufficient boundary layer recovery for convective updrafts to form in this region (as the recovery needs to occur upwind). A further discussion about the role of large-scale advection is given in section 4.

Regardless of the mechanism responsible, the lower θ_e values left-of-shear of the southerly component shear cases are unfavorable for TC intensification because mechanical work (both wind-driven and thermodynamically driven) through air–sea enthalpy fluxes is required to generate the enhanced moisture needed to recover θ_e values before parcels reach the downshear quadrants. While an increase of 4–6 K in θ_e (difference in values between left-of-shear and right-of-shear quadrants) due to the air–sea enthalpy fluxes is feasible based on past case studies of convective downdrafts away from the eyewall (Molinari et al. 2013; Zhang et al. 2017; Wadler et al. 2018b; Rudzin et al. 2020), the low-θ_e air can also spiral inward toward the inner-core before fully recovering, reducing the ability for convection to form downshear, which can lead to subsequent reductions in TC intensity (Riemer et al. 2010; Zhang et al. 2017). Even if the boundary layer recovery process is insufficient, the enthalpy fluxes that parcels experience as they spiral inward is likely the reason that the θ_e asymmetries are less significant radially inward of $r^* = 2$.

The estimated total enthalpy flux[2] (Fig. 9, latent heat flux plus sensible heat flux) shows a similar wavenumber-1 asymmetry between the left-of-shear and right-of-shear quadrants for both shear direction groups, with values generally greater

[1] The analyses in Fig. 7 are not truly shear relative since only the median shear vector for each group is plotted. However, the results in a normalized shear-relative framework showed nearly identical results (not shown).

[2] The enthalpy flux is likely underestimated since the buoy measurements are only recorded for 8 min of each hour, which would tend to undersample the strongest winds, especially in the inner core. Additionally, with fixed-length platforms that are often tilted in high-wind hurricane conditions, the measurements are not at the standard 10-m altitude. Even with these restrictions, however, the total enthalpy flux provides a reasonable and non-sample-biased estimate of the distributions of the fields.

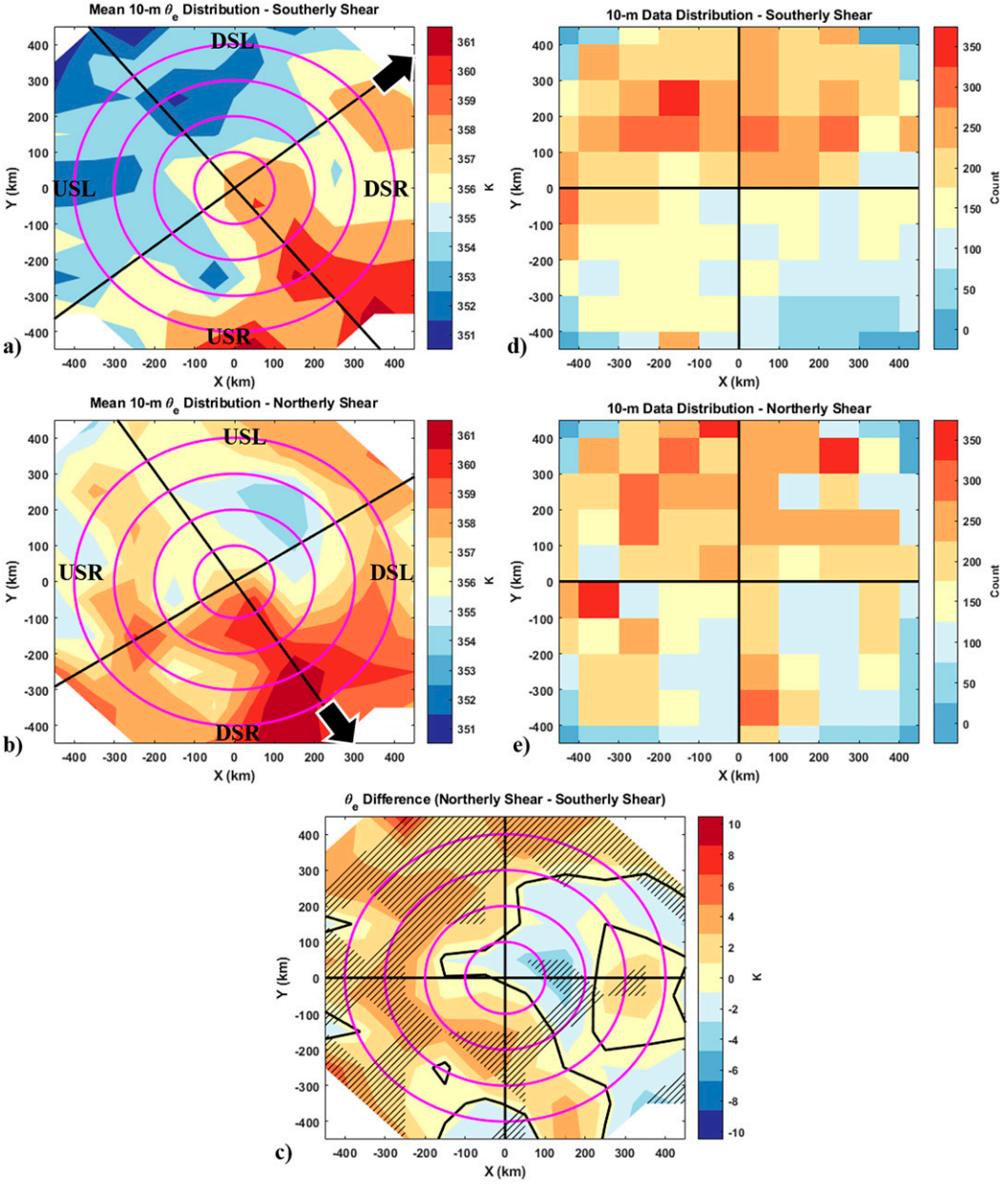

FIG. 7. The distribution of near-surface θ_e values for TCs experiencing (a) southerly component shear and (b) northerly component shear. In both (a) and (b), the data are grouped into bins with grid size of 100 km. In both (a) and (b) the median shear vector is plotted and the shear-relative DSR, DSL, USL, and USR quadrants are outlined. (c) The difference between (b) and (a), with statically significant differences at 95% hashed. The four pink range rings in (a)–(c) represent radial rings of 100–400 km. (d),(e) The data distributions for (a) and (b), respectively. Note that no means are computed for bins with less than 40 data points.

than 225 W m^{-2} radially outward of $r^* = 2$ left-of-shear and values lower than 200 W m^{-2} right-of-shear. While likely an underestimate (see footnote), the relatively low magnitudes of the enthalpy fluxes in the southerly component shear cases, particularly in the USR quadrant, which also has negative θ_e advection (Fig. 8a), likely means that the boundary layer θ_e values do not always fully recover from the low values left-of-shear before reaching the downshear quadrants. Note that enhanced enthalpy fluxes in this quadrant are shown to be favorable for intensification in a dropsonde composite study of weak TCs by Nguyen et al. (2019).

To test this hypothesis further, the southerly component shear cases were broken up into those that underwent 5-kt-or-greater strengthening or weakening in the subsequent 12 h. The mean upshear enthalpy flux radially inward of $r^* = 6$ for strengthening and weakening TCs is 246 and 212 W m^{-2}. The

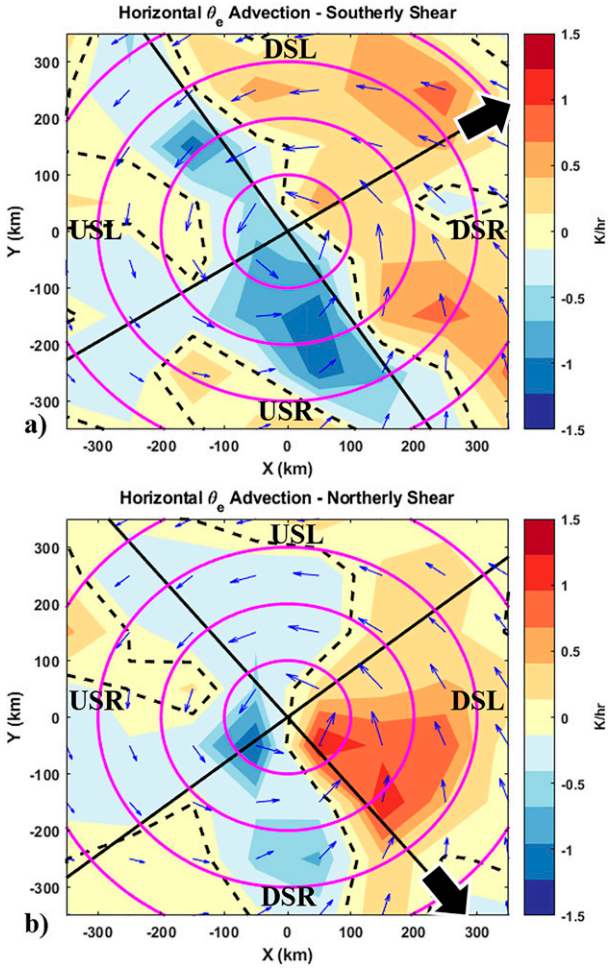

FIG. 8. As in Figs. 7a and 7b, but for horizontal θ_e advection. In both panels, 10-m wind vectors are overlaid. Note that the domain is reduced here relative to Fig. 7 because the finite-difference method of estimating a derivative eliminates the outermost grid point in both directions.

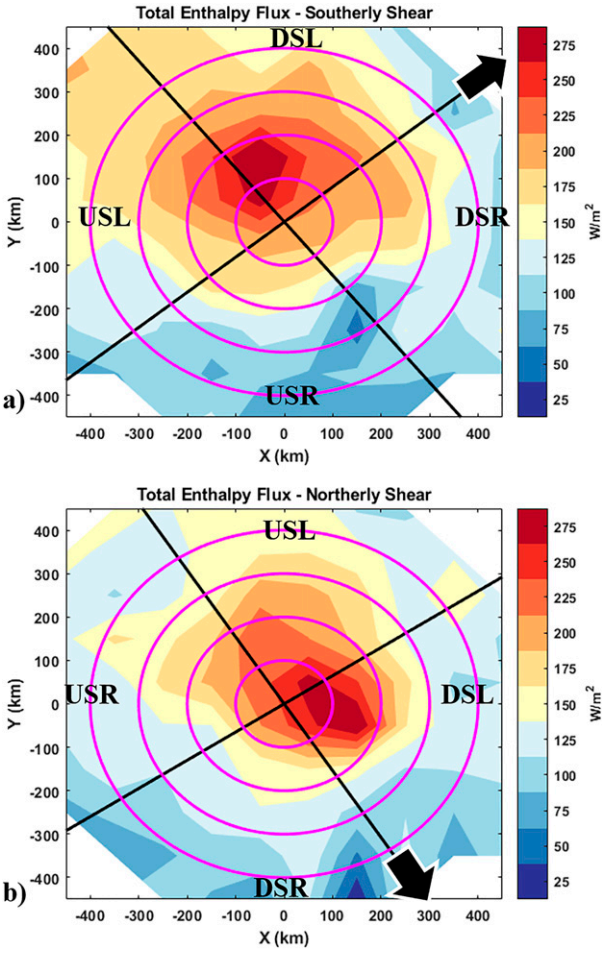

FIG. 9. As in Figs. 7a and 7b, but for total enthalpy (latent heat plus sensible heat) flux.

statistically significant (at 90% confidence interval) 16% increase in upshear enthalpy flux demonstrates that when a θ_e asymmetry is present, the magnitude of the enthalpy flux can determine whether boundary layer θ_e values recover between the left-of-shear and right-of-shear quadrants, which can directly influence the TC intensification rate. Likely associated with the lack of boundary layer recovery, 15.2% of the TC observations in the TCBD experiencing southerly component shear undergo subsequent weakening, relative to 9.8% of the northerly component shear cases that undergo subsequent weakening. Conversely, 27.5% of the TC observations in the TCBD experiencing southerly component shear undergo subsequent strengthening (same intensity change criteria as above), relative to 34% of the northerly component shear cases that undergo subsequent strengthening.

To emphasize the unfavorable nature of the southerly component shear thermodynamic and enthalpy flux distributions, the TCBD was recategorized for TCs that underwent intensification (>5-kt intensity change over the subsequent 12 h) and those that underwent weakening (<−5-kt intensity change over the subsequent 12 h), regardless of shear direction (sample sizes were too small to show distributions when the data were stratified by both shear direction and intensity change). The TCs that underwent weakening exhibited large asymmetries in θ_e (Fig. 10a) that resemble those in the southerly component shear cases (Fig. 4a). The weakening TCs had greater boundary layer θ_e asymmetries (i.e., the USL quadrant having the lowest θ_e of ~352–353 K, while the DSR having the largest θ_e of ~358–360 K), even though their initial intensity was larger (81.6 kt for weakening TCs vs 60.4 kt for intensifying TCs). While the differences between the USR and DSL quadrants are not significant, the differences in θ_e values between the DSR and USL quadrants emphasizes the unfavorable nature of requiring the boundary layer to recover θ_e between those regions. The favorable distribution of boundary layer θ_e in northerly component shear cases (Fig. 4b) resembles the distribution of TCs that underwent intensification (Fig. 10b). Between $r^* = 2$ and $r^* = 8$ in all quadrants, TCs that

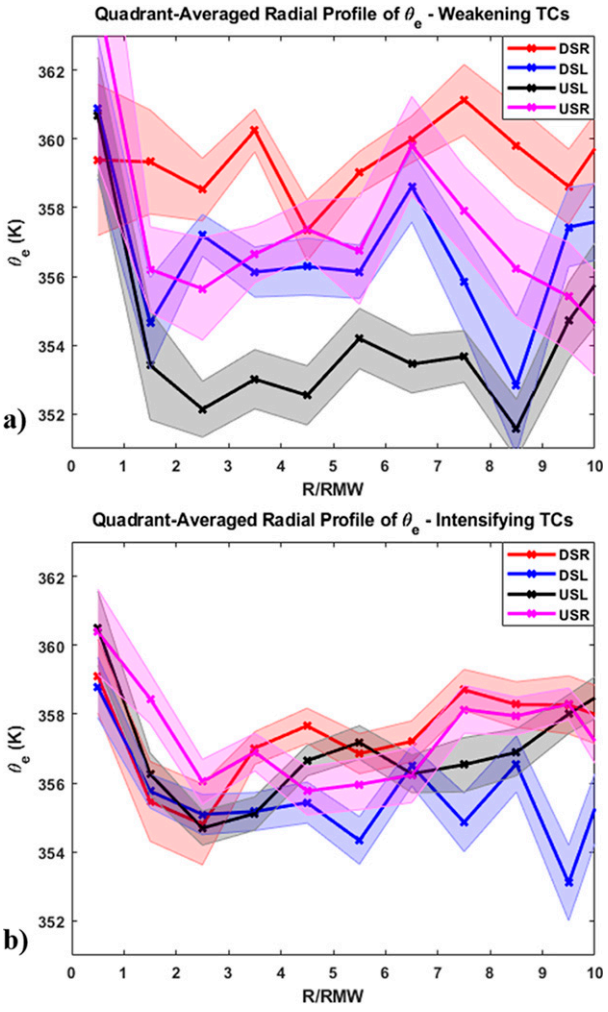

FIG. 10. As in Fig. 4, but for (a) weakening TCs and (b) intensifying TCs.

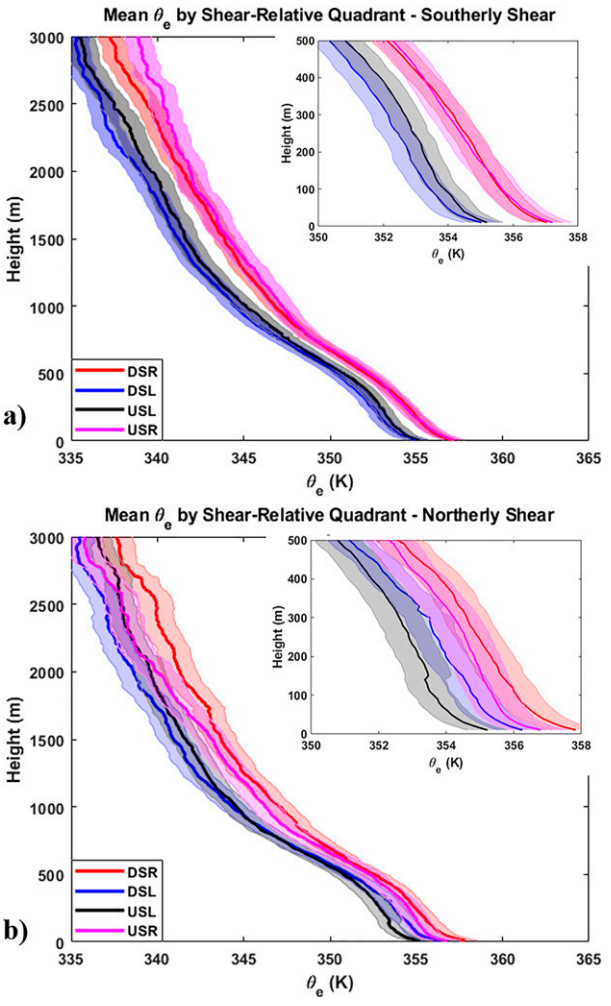

FIG. 11. Vertical profiles of quadrant-averaged θ_e from dropsonde observations outside $r^* = 2$ for TCs experiencing (a) southerly component shear and (b) northerly component shear. In both panels, the quadrant averaging is relative to the deep-layer environmental wind shear with the DSR, DSL, USL, and USR quadrants outlined. The profiles zoomed into the lowest 500 m are embedded in the top right of each panel. Shading for each line is 2 times the standard error in each direction.

underwent intensification had mean θ_e values between 355 and 358 K, with no clear asymmetry.

b. *Dropsonde analyses*

The dropsonde database, composed of measurements that are independent of the TCBD, shows a remarkably similar θ_e difference between the left-of-shear and right-of-shear quadrants (Fig. 11). In the southerly component shear cases (Fig. 11a), outside of $r^* = 2$, the 10-m average θ_e in the right-of-shear and left-of-shear quadrants is 357.1 and 355.1 K, respectively. Interestingly, the statistically significant differences between the left- and right-of-shear quadrants extend all the way to 3000-m altitude, signaling that the distinct asymmetries noticed outside $r^* = 2$ at 10-m altitude are not only from surface-based processes. As with the TCBD analyses, and other studies of downdraft ventilation in TCs (e.g., Zhang et al. 2017; Wadler et al. 2018b, 2021a,b; Nguyen et al. 2019), the differences in θ_e between the shear-relative quadrants largely resembles differences in atmospheric moisture (not shown).

In the northerly component shear cases (Fig. 11b), the average dropsonde profiles at 10-m altitude show some separation between the quadrants, though the gradient between the left-of-shear to right-of-shear quadrants is reduced. For example, parcels traveling from the DSR quadrant to the DSL quadrant in the northerly component shear cases do not experience as much of a θ_e reduction as in the southerly component shear cases. The only statistically significant difference at 10 m is between the DSR and USL quadrants, which have mean 10-m θ_e values of 357.8 and 355.2 K, respectively. This reduced θ_e asymmetry between the left-of-shear and right-of-shear quadrants of the northerly component shear cases is consistent throughout the lowest 500-m, but the differences become less robust above that altitude. Above ~1 km altitude, there is a separation between the left-of-shear and right-of-

shear quadrants, although not as robust as in the southerly component shear cases.

Another interesting aspect of the dropsonde profiles is a difference in the vertical θ_e gradient between the northerly component and southerly component shear cases (Fig. 12). While both negative, the vertical θ_e gradient is larger (more negative) in all quadrants between 500- and 1000-m altitude for the northerly component shear cases, meaning these profiles have more potential instability, favoring the growth of surface-based convection. Recall that, since all of these dropsondes are outside of $r^* = 2$, the increased convective instability in the northerly component shear cases can lead to stronger rainband convection. It is currently an open question if enhanced rainband activity is favorable for intensification. For example, enhanced rainband activity can negatively lead to low-θ_e air transferred to the boundary layer (e.g., Riemer et al. 2010). However, strong rainbands can help a TC resist dry air intrusion (Kimball 2006) and be a significant source of potential vorticity for the eyewall (e.g., Carr and Williams 1989; Montgomery and Kallenbach 1997; Nolan and Farrell 1999). A more comprehensive discussion about the role of rainbands for TC intensity can be found in in Wang (2009) and Moon and Nolan (2010).

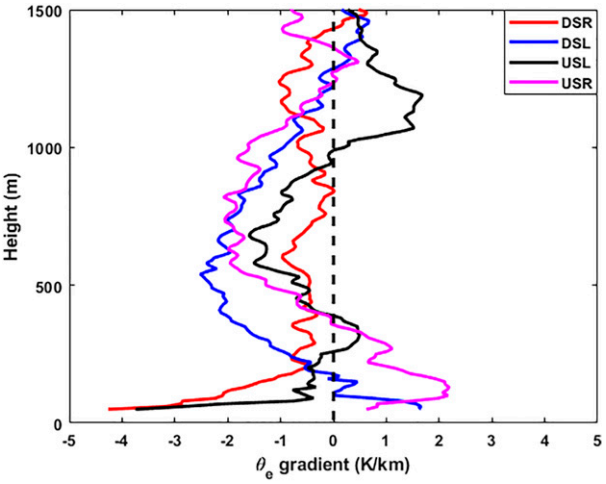

FIG. 12. Difference (northerly component shear − southerly component shear) in vertical gradient of quadrant-averaged θ_e for each shear-relative quadrant from dropsonde profiles radially outward of $r^* = 2$. All profiles are smoothed by a 50-point moving average. The vertical black dashed line outlines zero difference.

c. SHIPS

With the SHIPS developmental database updated at 6-h intervals for every tropical system, the predictors and environmental variables in the database essentially represent a climatology over the years to which they are estimated (1982–2017). The population distributions of selected environmental variables are given in Fig. 13 for both TCs experiencing northerly component and southerly component shear. Generally, northerly component shear cases exhibit a more favorable environment, consistent with what was found in both the TCBD and dropsonde composites. The mean SST (Fig. 13a) for northerly component shear cases is 28.5°C, and the mean SST (Fig. 13a) for southerly component shear cases is 28.3°C, while the mean deep-layer wind shear magnitude (Fig. 13b) is 13.8 and 15.5 kt, respectively. Both differences are statistically significant at 99.9% confidence interval. In contrast, averaged RH between 850 and 700 hPa (Fig. 13c) show no statistically significant differences. There are also no differences in average RH between 700–500 and 500–300 hPa (not shown). The θ_e at 1000 hPa (Fig. 13d), averaged in an annulus between 200 and 800 km, shows a ~1 K higher value in northerly component shear cases, which is also statistically significant at 99.9%, and resembles the results shown in the TCBD analyses.

With a favorability in mean environmental characteristics for northerly component shear cases, the mean 6-h subsequent intensity change (Fig. 14a) for northerly component and southerly component shear cases is 2.3 and 1.6 kt, respectively. The difference in intensification rate is more apparent at 12 h (Fig. 14b), as the mean subsequent intensity change for northerly component and southerly component shear cases is 4.4 and 2.8 kt, respectively. The normalized (by the total case number) distributions demonstrate a clear preference for northerly component or southerly component cases to undergo subsequent intensification or weakening, respectively, further emphasizing the mean difference of 1.6 kt in mean 12-h intensity change between the shear directions groups. Interestingly, the differences between northerly component and southerly component shear are maximized in the moderate shear range (Fig. 14c), defined as a shear magnitude between 4.5 and 11.0 ms^{-1}, which is one of the most challenging environmental regimes for TC intensity forecasting (Molinari et al. 2004, 2006; Molinari and Vollaro 2010; Montgomery et al. 2010; Bhatia and Nolan 2013; Foerster et al. 2014; Stevenson et al. 2014; Rios-Berrios et al. 2016b,a; Zawislak et al. 2016; Rios-Berrios and Torn 2017; Nguyen et al. 2017; Finocchio and Majumdar 2017; Rios-Berrios et al. 2018; Rogers et al. 2020). In this regime, the difference in mean 12-h subsequent intensity change is 1.6 kt (statistically significant at over 99.9%). The normalized distribution for TCs experiencing moderate wind shear shows a stronger preference for intensification for the northerly component shear cases, especially when the subsequent intensity change is between 0 and 20 kt (mean shear magnitude for these cases is 14.7 kt in northerly component shear and 15.1 kt in southerly component shear cases). The southerly component shear cases show a stronger preference for weakening between a subsequent intensity change of −20 and 0 kt (mean shear magnitude for these cases is 15.3 kt for northerly component shear and 15.5 kt for southerly component shear cases).

A closer look at the shear direction emphasizes its relationship with 6- and 12-h TC intensity change (Fig. 15). For 6-h intensity change for TCs in moderate shear (Fig. 15a), weakening TCs (defined as <-10-kt subsequent intensity change) occur most frequently when the shear heading is 30°–60° (more likely to characterize the environment of an approaching trough). In contrast, intensifying TCs (defined as >10-kt subsequent intensity change) occur most frequently when the shear heading is 90°–120° (more likely to characterize the environment of an approaching ridge). The median shear headings for intensifying and weakening TCs in moderate shear are 107.5° and 77°, respectively. This difference is also seen when examining 12-h subsequent intensity change (Fig. 15b). While at this intensity change

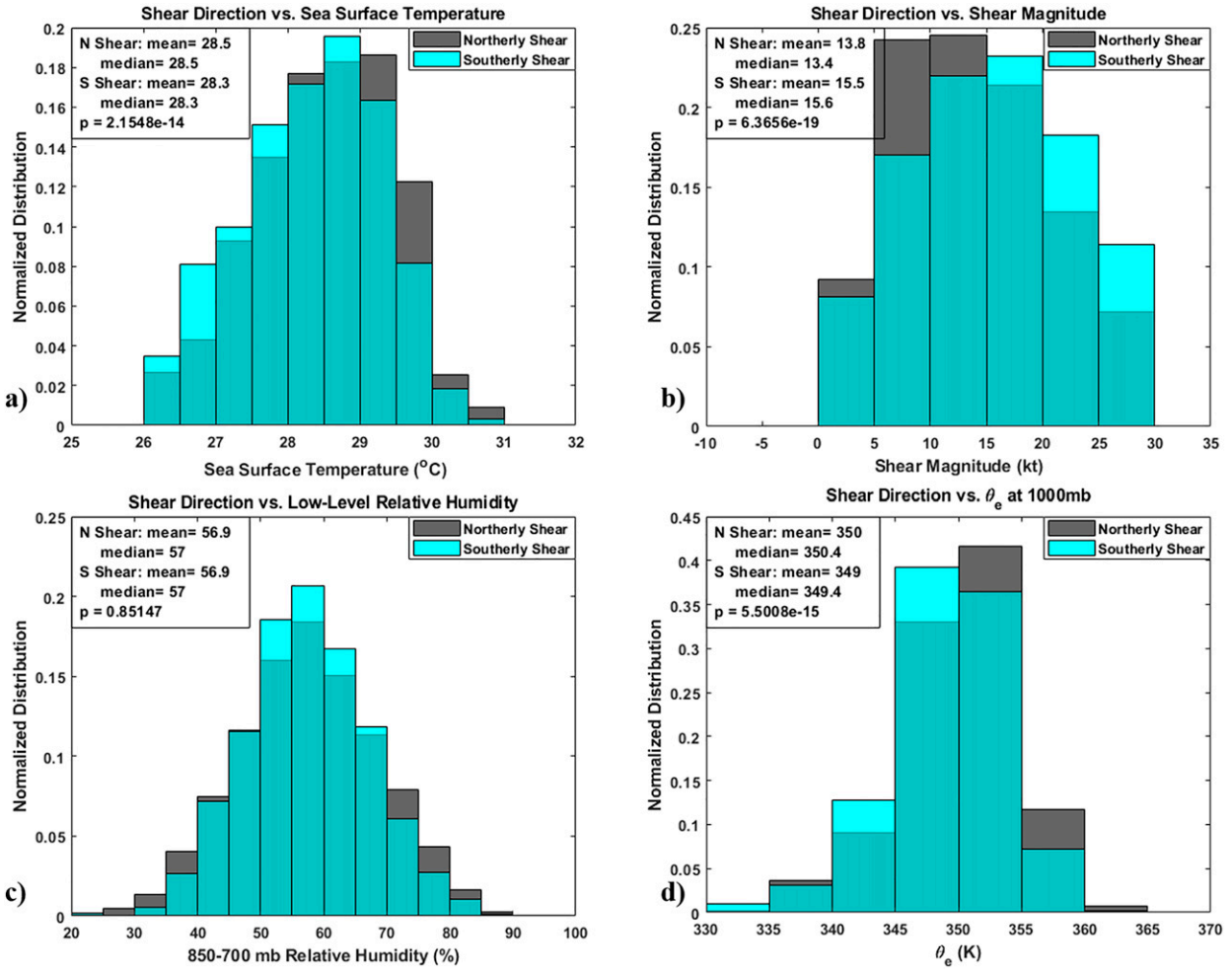

FIG. 13. Histograms for the relative distributions of (a) sea surface temperature, (b) deep-layer wind shear magnitude, (c) 850–700-hPa relative humidity, and (d) 1000-hPa θ_e for all TCs experiencing northerly component and southerly component shear in the SHIPS database. In each panel, the mean and median for each group as well as the p value from the Student's t test are displayed. Note that since these are relative distributions the ordinate axis is different in each panel.

interval the weakening TCs (same intensity change criteria) occur most frequently at a shear heading of 60°–90°, a clockwise rotation of the preferential shear heading from that at 6-h intensity change, intensifying TCs still occur most frequently with a 90°–120° shear heading. Additionally, the median shear headings of 109° and 77° between intensifying and weakening TCs, respectively, is remarkably similar to that from that at 6-h intensity change. Note that these differences also appear when considering TCs in all shear magnitudes, but the differences are not as significant as in the moderate shear cases (not shown).

4. Discussion and conclusions

The relationship between deep-layer environmental wind shear and the distribution of TC boundary layer thermodynamics is explored using multiple independent datasets. Previous studies of TC genesis showed that easterly shear is statistically more favorable than westerly shear (Tuleya and Kurihara 1981), but that may be due to easterly shear occurring in more favorable environmental thermodynamic conditions (Nolan and McGauley 2012). A previous study of developed storms showed that TCs experiencing southerly component shear have higher atmospheric specific humidity values downshear and right-of-shear, but TCs experiencing northerly component shear have more symmetric moisture distributions (Cione et al. 2013). In this study, analyses derived from the tropical cyclone buoy database, which contains information from TCs in the western Atlantic basin between 1978 and 2017, show that the primary difference in the near-surface thermodynamics between TCs experiencing northerly component and southerly component shear is the degree of asymmetry between the left-of-shear and right-of-shear quadrants. When TCs are experiencing southerly component shear, there is a wavenumber-1 asymmetry in the θ_e distribution between $r^* = 2$ and $r^* = 10$, with the values

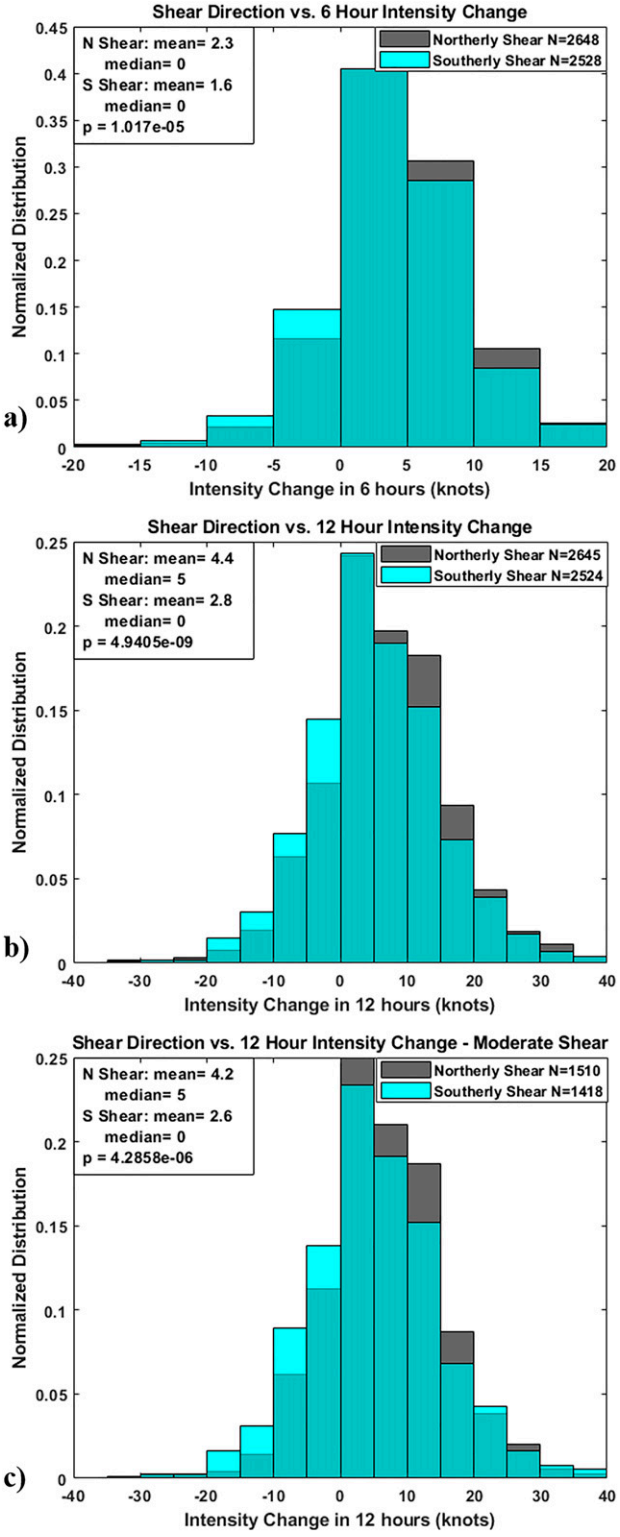

FIG. 14. Histograms for the relative distributions of (a) 6-h TC intensity change, (b) 12-h TC intensity change, and (c) 12-h TC intensity change when the wind shear magnitude was in the moderate range (between 4.5 and 11.0 m s^{-1}) for all TCs experiencing northerly component and southerly component shear in the SHIPS database. In each panel, the mean and median for each group as well as the p value from the Student's t test are displayed. Note that since these are relative distributions the ordinate axis is different in each panel.

at each radial band in the left-of-shear quadrants ranging generally between 352 and 355 K, while the values in the right-of-shear quadrants are generally between 356 and 359 K. The low θ_e values in the left-of-shear quadrants correspond with the northwest area of the TC. In contrast, the θ_e distribution is less asymmetric when TCs experience northerly component shear, with values at each radial band ranging between 355 and 359 K (though the values are slightly lower in the northwest and generally upshear quadrant). The differences in θ_e likely are maximized radially outward of $r^* = 2$ because as air spirals inward, the air–sea enthalpy fluxes lead to boundary layer recovery of θ_e values (e.g., Alland et al. 2021a, Wadler et al. 2021b). This reduces the thermodynamic asymmetry, even if the boundary layer recovery is insufficient (discussed further below). Of note, no significant differences in the SST or wind speed distributions were noticed between the two shear direction groups.

Similar 10-m θ_e distributions were noticed outside $r^* = 2$ from analyses derived from an independent dropsonde database, highlighting the robustness of these differences between TCs experiencing northerly component and southerly component shear. In the dropsonde database, the asymmetry in θ_e between the left-of-shear and right-of-shear quadrants observed at 10-m altitude for TCs experiencing southerly component shear generally remains statistically significant up to at least 3-km altitude (the highest altitude of the dropsonde database). The reduced asymmetry between the quadrants in the TCs experiencing northerly component shear extends upward to 500-m altitude. In analyses from both the TCBD and dropsonde database, the signals noticed for θ_e largely resemble the distribution of atmospheric moisture, a similar result to previous observational studies (e.g., Zhang et al. 2017; Wadler et al. 2018b, 2021a; Nguyen et al. 2019). A composite study about how these thermodynamic asymmetries relate to precipitation distributions is ongoing.

Since the buoy data are biased toward nearshore regions and north of 20°N, and the θ_e signals extend over a large area and outward to $r^* = 10$, we hypothesize that the superposition between the location of convective downdrafts with horizontal large-scale advection is responsible for the different distributions (Fig. 16). For both shear direction groups, the largest θ_e values are in the southeast quadrant, making the biggest difference between them the low-θ_e values in the northwest quadrant of TCs experiencing southerly component shear. With a median shear heading of 51° for southerly component cases (Fig. 16a), poleward transport of moist-tropical air that is typical on the eastern side of TCs coincides with the right-of-shear quadrants (there is positive θ_e advection throughout the downshear quadrants), which are characterized by a moist inflow layer in the region typically associated with convective initiation and low-level convergence (e.g., Reasor et al. 2013; DeHart et al. 2014). The equatorward transport of cooler/drier subtropical air that is

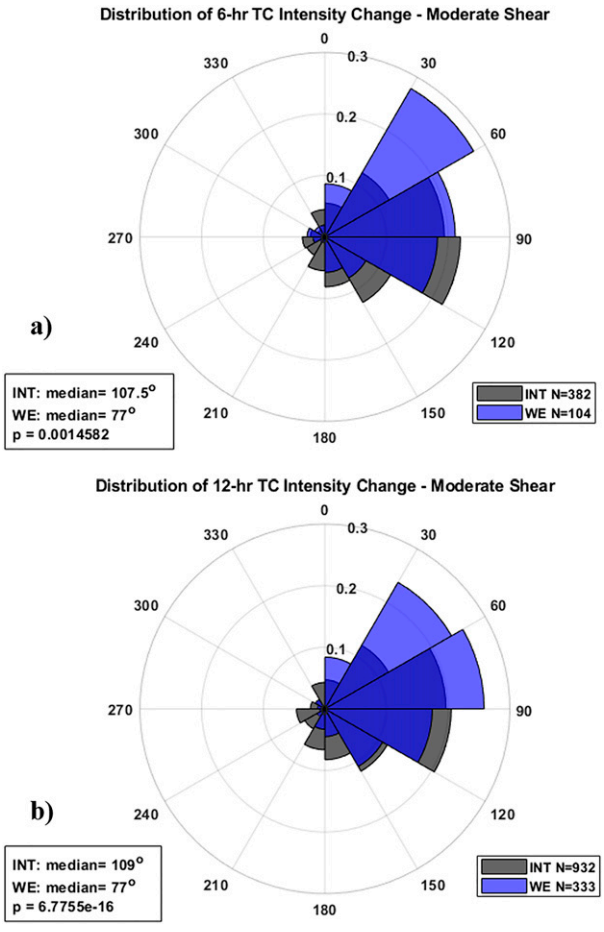

FIG. 15. Polar histograms for the relative distributions of shear heading based on (a) 6-h intensity change when the wind shear magnitude was in the moderate range (between 4.5 and 11.0 m s^{-1}) and (b) 12-h intensity change when the wind shear magnitude was in the moderate range. In both panels, the median for each group as well as the p value from the Student's t test are displayed.

typical of the western side of TCs coincides with the left-of-shear quadrants (there is negative θ_e advection throughout the upshear quadrants), which are the characterized by outer-core convective downdrafts that transport low θ_e air to the boundary layer (i.e., Riemer et al. 2010). The superposition of subtropical air with that from downdraft ventilation creates a particularly unfavorable thermodynamic environment in this region. Note that since the low θ_e air extends radially outward to $r^* = 10$, convective downdrafts, which are typically concentrated in rainbands near $r^* = 2$–3 (e.g., Wang 2009), cannot be fully responsible for the signal. Additionally, since the mean shear magnitudes between the shear direction groups are comparable, the more widespread low θ_e air in TCs exposed to southerly component shear are unlikely to be due to a larger vertical-tilt and more downward motions upshear.

With a median shear heading of 147°, the region of convective downdrafts for TCs experiencing northerly component shear coincides with the areas of poleward transport of moist-tropical air (Fig. 16b; largest positive θ_e advection is in the DSL quadrant). The moisture transport may limit the negative effects of the downdrafts in the left-of-shear quadrants (and limit the need for rapid recovery of the low-θ_e air via the surface enthalpy fluxes) and lead to θ_e values that are more comparable to those in the right-of-shear quadrants, which feature equatorward advection of drier subtropical air (there is negative θ_e advection through most areas of the right-of-shear quadrants). While the differences between the two groups are robust and shown in multiple independent observational databases, further evaluation of our findings can be done using idealized numerical simulations and future case studies with targeted observations near outer-core convective downdrafts. Such studies can directly link specific structures such as mesoscale/convective downdrafts and large-scale synoptic flow with the distribution of boundary layer thermodynamics and subsequent θ_e evolution as air spirals inward from radially outward of $r^* = 2$ to the inner core. Additionally, the large-scale flow described for the northerly component and southerly component shear cases should be most prominent in the subtropics, as TCs approach the northwestern part of the Atlantic basin. The primary signals are reflective of TCs that are north of 20°N latitude or west of 65°W longitude (not shown), but the sample sizes are much smaller when the geographic region is reduced. A study about the preferential geographic locations of these thermodynamic distributions under different shear regimes is a topic of future work.

The more symmetric distribution of boundary layer thermodynamics in the northerly component shear cases is favorable for TC intensification. In these cases, less boundary layer recovery of θ_e values is required between the left-of-shear and right-of-shear quadrants, which increases the likelihood of high entropy air entering the eyewall downshear. The asymmetric θ_e distribution in the southerly component shear cases requires a boundary layer recovery of 4–6 K θ_e deficit throughout the depth of the boundary layer between the left-of-shear and right-of-shear quadrants. Previous case studies showed that the air–sea enthalpy fluxes can provide sufficient heating for boundary layer θ_e recovery as air spirals inward from the region of convective downdrafts to the RMW of intensifying TCs (Zhang et al. 2017; Wadler et al. 2018a, 2021b; Rudzin et al. 2020), but the low entropy air can also enter the eyewall region and cause a storm to weaken, especially when the shear is large and the downdrafts are widespread (Riemer et al. 2010). It is likely that the magnitude of the enthalpy fluxes and the efficiency of boundary layer recovery plays a critical role in determining whether a storm will intensify. Our results showed that TCs exposed to southerly component shear that underwent subsequent strengthening experiencing 16% higher total enthalpy flux in the upshear quadrants (signifying more recovery) than those that underwent subsequent weakening. Future studies are recommended to evaluate the boundary layer recovery processes in TCs with different size and strength in both shear-relative and storm-relative frameworks.

The unfavorable thermodynamic distributions and less overall favorable environmental conditions of the southerly component shear cases are reflected in the SHIPS developmental database. Analyses from this database showed that strengthening storms

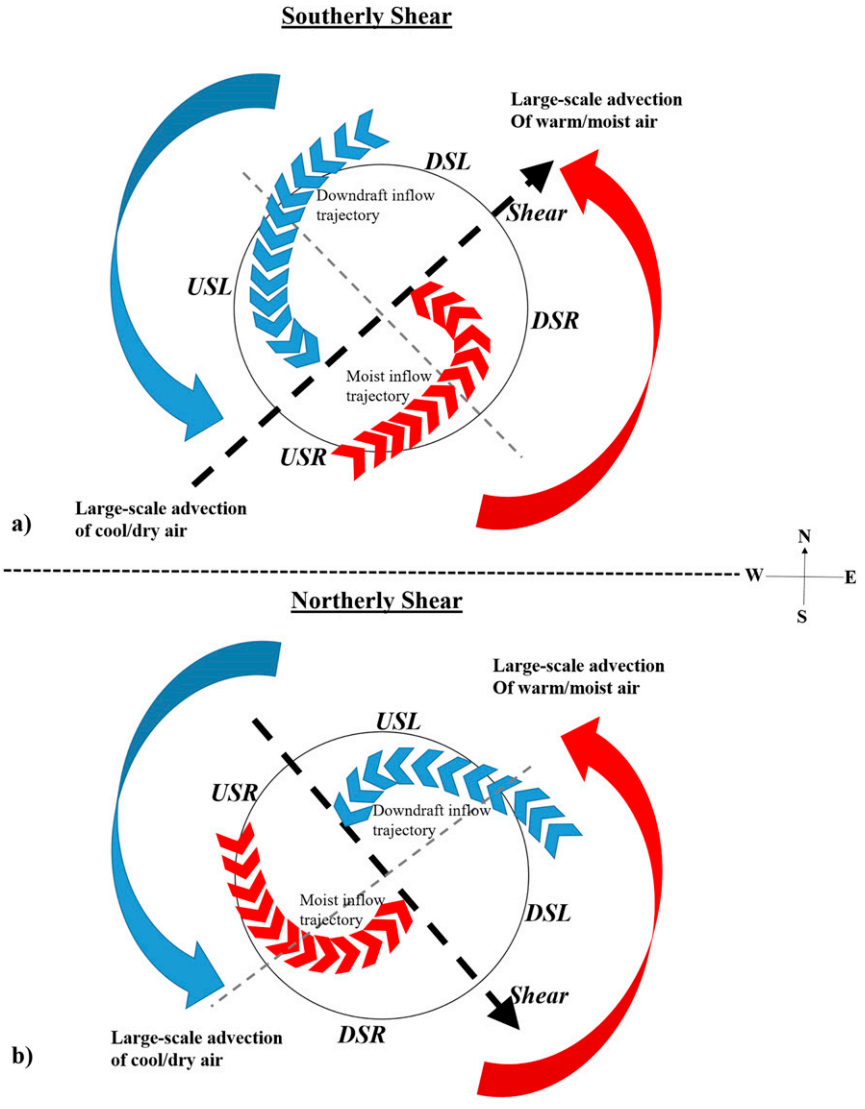

FIG. 16. Schematic of the hypothesized environmental setup that leads to the boundary layer thermodynamic distributions in TCs experiencing (a) southerly component shear and (b) northerly component shear. The red and blue arrows correspond to regions of high and low θ_e air, respectively.

favor northerly component shear whereas weakening storms favor southerly component shear at both 6- and 12-h subsequent intensity change intervals. The differences in intensity change were maximized in the moderate shear (4.5–11.0 m s^{-1}) range, with subsequently strengthening TCs occurring at the highest frequency when the shear heading is between 90° and 120° and subsequently weakening TCs occurring at the highest frequency when the shear heading is between 30° and 60°. These statistically significant differences highlight the detrimental impact that thermodynamic asymmetry can have on TC intensity, as the mean axisymmetric RH shows no statistically significant differences between the shear directions groups at any altitude. Potentially, the shear headings may also represent synoptic environments of approaching troughs (heading of 30°–60°) or ridges (heading of 90°–120°), since a trough's winds extend deeper through the troposphere, a pattern noticed to be more detrimental to a TCs intensity (Elsberry and Jeffries 1996; Velden and Sears 2014; Finocchio et al. 2016; Ryglicki et al. 2018). The specific relationship between the degree of thermodynamic asymmetry with shear direction, the depth of the shear, and the synoptic environment is a topic of future work using global reanalysis datasets where multiple wind shear metrics can be calculated. Additionally, future work should consider how gradients in the environmental parameters can lead to ventilation of air mass into different geographic regions of TCs that may have varying influence on the shear-induced asymmetries.

Our results highlight how deep-layer wind shear direction influences future TC intensity changes through the distribution

of outer-core boundary layer thermodynamics. These relationships can be utilized as an additional forecasting tool, especially in moderate wind shear regimes, which are a challenge to forecast TC intensity. To further elucidate the processes controlling boundary layer thermodynamic variability, both observational and numerical case studies are needed. Observational studies would require extensive sampling of the boundary layer outside the inner core of a TC, especially near convectively active regions, which can be done with an uncrewed aircraft (e.g., Cione et al. 2020) in combination with dropsonde and radar observations. These observations could be directly assimilated into numerical weather prediction models to enhance the accuracy of TC model initialization. Last, these observations can be used to create an operational analysis product that can be viewed by forecasters and will eventually lead to development of a new thermal predictor for the operational SHIPS RI system to improve TC intensity change prediction.

Acknowledgments. The authors thank the comments from three anonymous reviewers, which significantly helped to improve the presentation of the results and clarity of the paper. This research was carried out (in part) under the auspices of the Cooperative Institute for Marine and Atmospheric Studies (CIMAS), a Cooperative Institute of the University of Miami and the National Oceanic and Atmospheric Administration, Cooperative Agreement NA20OAR4320472. The authors appreciate the comments from Drs. Robert Rogers and Frank Marks of NOAA/HRD, which helped to improve the paper. Evan Kalina is supported by funding from NOAA Award NA17OAR4320101. Jun Zhang is supported by funding from ONR Award N00014-20-1-2071.

Data availability statement. Parties interested in obtaining observations associated with the TCBD should contact Joseph Cione (joe.cione@noaa.gov), and parties interested in obtaining the dropsonde database should contact Jun Zhang (jun.zhang@noaa.gov).

REFERENCES

Alland, J. J., B. H. Tang, and K. L. Corbosiero, 2017: Effects of mid-level dry air on development of the axisymmetric tropical cyclone secondary circulation. *J. Atmos. Sci.*, **74**, 1455–1470, https://doi.org/10.1175/JAS-D-16-0271.1.

——, ——, ——, and G. H. Bryan, 2021a: Synergistic effects of midlevel dry air and vertical wind shear on tropical cyclone development. Part I: Downdraft ventilation. *J. Atmos. Sci.*, **78**, 763–782, https://doi.org/10.1175/JAS-D-20-0054.1.

——, ——, ——, and ——, 2021b: Combined effects of midlevel dry air and vertical wind shear on tropical cyclone development. Part II: Radial ventilation. *J. Atmos. Sci.*, **78**, 783–796, https://doi.org/10.1175/JAS-D-20-0055.1.

Alvey, G. R., III, J. Zawislak, and E. Zipser, 2015: Precipitation properties observed during tropical cyclone intensity change. *Mon. Wea. Rev.*, **143**, 4476–4492, https://doi.org/10.1175/MWR-D-15-0065.1.

——, E. Zipser, and J. Zawislak, 2020: How does Hurricane Edouard (2014) evolve toward symmetry before rapid intensification? A high-resolution ensemble study. *J. Atmos. Sci.*, **77**, 1329–1351, https://doi.org/10.1175/JAS-D-18-0355.1.

Bhatia, K. T., and D. S. Nolan, 2013: Relating the skill of tropical cyclone intensity forecasts to the synoptic environment. *Wea. Forecasting*, **28**, 961–980, https://doi.org/10.1175/WAF-D-12-00110.1.

Carr, L. E., and R. T. Williams, 1989: Barotropic vortex stability to perturbations from axisymmetry. *J. Atmos. Sci.*, **46**, 3177–3191, https://doi.org/10.1175/1520-0469(1989)046<3177:BVSTPF>2.0.CO;2.

Chen, B., C. A. Davis, and Y. Kuo, 2018: Effects of low-level flow orientation and vertical shear on the structure and intensity of tropical cyclones. *Mon. Wea. Rev.*, **146**, 2447–2467, https://doi.org/10.1175/MWR-D-17-0379.1.

——, ——, and ——, 2019: An idealized numerical study of shear-relative low-level mean flow on tropical cyclone intensity and size. *J. Atmos. Sci.*, **76**, 2309–2334, https://doi.org/10.1175/JAS-D-18-0315.1.

Chen, H., and S. G. Gopalakrishnan, 2015: A study on the asymmetric rapid intensification of Hurricane Earl (2010) using the HWRF system. *J. Atmos. Sci.*, **72**, 531–550, https://doi.org/10.1175/JAS-D-14-0097.1.

Chen, X., J. Gu, J. A. Zhang, F. D. Marks, R. F. Rogers, and J. J. Cione, 2021: Boundary layer recovery and precipitation symmetrization preceding rapid intensification of tropical cyclones under shear. *J. Atmos. Sci.*, **78**, 1523–1544, https://doi.org/10.1175/JAS-D-20-0252.1.

Cione, J. J., 2015: The relative roles of the ocean and atmosphere as revealed by buoy air–sea observations in hurricanes. *Mon. Wea. Rev.*, **143**, 904–913, https://doi.org/10.1175/MWR-D-13-00380.1.

——, and E. W. Uhlhorn, 2003: Sea surface temperature variability in hurricanes: Implications with respect to intensity change. *Mon. Wea. Rev.*, **131**, 1783–1796, https://doi.org/10.1175//2562.1.

——, P. G. Black, and S. H. Houston, 2000: Surface observations in the hurricane environment. *Mon. Wea. Rev.*, **128**, 1550–1561, https://doi.org/10.1175/1520-0493(2000)128<1550:SOITHE>2.0.CO;2.

——, E. A. Kalina, J. A. Zhang, and E. W. Uhlhorn, 2013: Observations of air–sea interaction and intensity change in hurricanes. *Mon. Wea. Rev.*, **141**, 2368–2382, https://doi.org/10.1175/MWR-D-12-00070.1.

——, and Coauthors, 2020: Eye of the storm: Observing hurricanes with a small unmanned aircraft system. *Bull. Amer. Meteor. Soc.*, **101**, E186–E205, https://doi.org/10.1175/BAMS-D-19-0169.1.

Davis, C. A., 2018: Resolving tropical cyclone intensity in models. *Geophys. Res. Lett.*, **45**, 2082–2087, https://doi.org/10.1002/2017GL076966.

DeHart, J. C., R. A. Houze, and R. F. Rogers, 2014: Quadrant distribution of tropical cyclone inner-core kinematics in relation to environmental shear. *J. Atmos. Sci.*, **71**, 2713–2732, https://doi.org/10.1175/JAS-D-13-0298.1.

DeMaria, M., M. Mainelli, L. K. Shay, J. A. Knaff, and J. Kaplan, 2005: Further improvements in the Statistical Hurricane Intensity Prediction Scheme (SHIPS). *Wea. Forecasting*, **20**, 531–543, https://doi.org/10.1175/WAF862.1.

——, C. R. Sampson, J. A. Knaff, and K. D. Musgrave, 2014: Is tropical cyclone intensity guidance improving? *Bull. Amer. Meteor. Soc.*, **95**, 387–398, https://doi.org/10.1175/BAMS-D-12-00240.1.

Demuth, J., M. DeMaria, and J. A. Knaff, 2006: Improvement of Advanced Microwave Sounder Unit tropical cyclone intensity and size estimation algorithms. *J. Appl. Meteor. Climatol.*, **45**, 1573–1581, https://doi.org/10.1175/JAM2429.1.

Elsberry, R. L., and R. A. Jeffries, 1996: Vertical wind shear influences on tropical cyclone formation and intensification during TCM-92 and TCM-93. *Mon. Wea. Rev.*, **124**, 1374–1387, https://doi.org/10.1175/1520-0493(1996)124<1374:VWSIOT>2.0.CO;2.

Finocchio, P. M., and S. J. Majumdar, 2017: The predictability of idealized tropical cyclones in environments with time-varying vertical wind shear. *J. Adv. Model. Earth Syst.*, **9**, 2836–2862, https://doi.org/10.1002/2017MS001168.

——, ——, D. S. Nolan, and M. Iskandarani, 2016: Idealized tropical cyclone responses to the height and depth of environmental vertical wind shear. *Mon. Wea. Rev.*, **144**, 2155–2175, https://doi.org/10.1175/MWR-D-15-0320.1.

Foerster, A. M., M. M. Bell, P. A. Harr, and S. C. Jones, 2014: Observations of the eyewall structure of Typhoon Sinlaku (2008) during the transformation stage of extratropical transition. *Mon. Wea. Rev.*, **142**, 3372–3392, https://doi.org/10.1175/MWR-D-13-00313.1.

Gilhousen, D. B., 1988: Quality control of meteorological data from automated marine stations. Preprints, *Fourth Int. Conf. on Interactive Information and Processing Systems for Meteorology, Oceanography, and Hydrology,* Miami, FL, Amer. Meteor. Soc., 113–117.

——, 1998: Improved real-time quality control of NDBC measurements. Preprints, *10th Symp. on Meteorological Observations and Instrumentation*, Phoenix, AZ, Amer. Meteor. Soc., 363–366.

Hazelton, A. T., R. Rogers, and R. E. Hart, 2015: Shear-relative asymmetries in tropical cyclone eyewall slope. *Mon. Wea. Rev.*, **143**, 883–903, https://doi.org/10.1175/MWR-D-14-00122.1.

Hock, T. F., and J. L. Franklin, 1999: The NCAR GPS dropwindsonde. *Bull. Amer. Meteor. Soc.*, **80**, 407–420, https://doi.org/10.1175/1520-0477(1999)080<0407:TNGD>2.0.CO;2.

Jaimes, B., and L. K. Shay, 2015: Enhanced wind-driven downwelling flow in warm oceanic eddy features during the intensification of Tropical Cyclone Isaac (2012): Observations and theory. *J. Phys. Oceanogr.*, **45**, 1667–1689, https://doi.org/10.1175/JPO-D-14-0176.1.

——, ——, and J. K. Brewster, 2016: Observed air-sea interactions in tropical cyclone Isaac over loop current mesoscale eddy features. *Dyn. Atmos. Oceans*, **76**, 306–324, https://doi.org/10.1016/j.dynatmoce.2016.03.001.

Jiang, H., 2012: The relationship between tropical cyclone intensity change and the strength of inner-core convection. *Mon. Wea. Rev.*, **140**, 1164–1176, https://doi.org/10.1175/MWR-D-11-00134.1.

——, J. P. Zagrodnik, C. Tao, and E. J. Zipser, 2018: Classifying precipitation types in tropical cyclones using the NRL 37 GHz color product. *J. Geophys. Res. Atmos.*, **123**, 5509–5524, https://doi.org/10.1029/2018JD028324.

Kieper, M., and H. Jiang, 2012: Predicting tropical cyclone rapid intensification using the 37 GHz ring pattern identified from passive microwave measurements. *Geophys. Res. Lett.*, **39**, L13804, https://doi.org/10.1029/2012GL052115.

Kimball, S., 2006: A modeling study of hurricane landfall in a dry environment. *Mon. Wea. Rev.*, **134**, 1901–1918, https://doi.org/10.1175/MWR3155.1.

Klotz, B. W., and E. W. Uhlhorn, 2014: Improved stepped frequency microwave radiometer tropical cyclone surface winds in heavy precipitation. *J. Atmos. Oceanic Technol.*, **31**, 2392–2408, https://doi.org/10.1175/JTECH-D-14-00028.1.

Klotzbach, P. J., S. G. Bowen, R. Pielke, and M. Bell, 2018: Continental U.S. hurricane landfall frequency and associated damage: Observations and future risks. *Bull. Amer. Meteor. Soc.*, **99**, 1359–1376, https://doi.org/10.1175/BAMS-D-17-0184.1.

Landsea, C. W., and J. L. Franklin, 2013: Atlantic hurricane database uncertainty and presentation of a new database format. *Mon. Wea. Rev.*, **141**, 3576–3592, https://doi.org/10.1175/MWR-D-12-00254.1.

Leighton, H., S. Gopalakrishnan, J. A. Zhang, R. F. Rogers, Z. Zhang, and V. Tallapragada, 2018: Azimuthal distribution of deep convection, environmental factors, and tropical cyclone rapid intensification: A perspective from HWRF ensemble forecasts of Hurricane Edouard (2014). *J. Atmos. Sci.*, **75**, 275–295, https://doi.org/10.1175/JAS-D-17-0171.1.

Marks, F., and L. K. Shay, 1998: Landfalling tropical cyclones: Forecast problems and associated research opportunities. *Bull. Amer. Meteor. Soc.*, **79**, 305–323, https://doi.org/10.1175/1520-0477(1998)079<0305:LTCFPA>2.0.CO;2.

Molinari, J., and D. Vollaro, 2010: Rapid intensification of a sheared tropical storm. *Mon. Wea. Rev.*, **138**, 3869–3885, https://doi.org/10.1175/2010MWR3378.1.

——, ——, and K. L. Corbosiero, 2004: Tropical cyclone formation in a sheared environment: A case study. *J. Atmos. Sci.*, **61**, 2493–2509, https://doi.org/10.1175/JAS3291.1.

——, P. Dodge, D. Vollaro, K. L. Corbosiero, and F. Marks Jr., 2006: Mesoscale aspects of the downshear reformation of a tropical cyclone. *J. Atmos. Sci.*, **63**, 341–354, https://doi.org/10.1175/JAS3591.1.

——, J. Frank, and D. Vollaro, 2013: Convective bursts, downdraft cooling, and boundary layer recovery in a sheared tropical storm. *Mon. Wea. Rev.*, **141**, 1048–1060, https://doi.org/10.1175/MWR-D-12-00135.1.

Montgomery, M. T., and R. J. Kallenbach, 1997: A theory for vortex Rossby-waves and its application to spiral bands and intensity changes in hurricanes. *Quart. J. Roy. Meteor. Soc.*, **123**, 435–465, https://doi.org/10.1002/qj.49712353810.

——, L. L. Lussier III, R. W. Moore, and Z. Wang, 2010: The genesis of Typhoon Nuri as observed during the Tropical Cyclone Structure 2008 (TCS-08) field experiment—Part 1: The role of the easterly wave critical layer. *Atmos. Chem. Phys.*, **10**, 9879–9900, https://doi.org/10.5194/acp-10-9879-2010.

Moon, Y., and D. S. Nolan, 2010: The dynamic response of the hurricane wind field to spiral rainband heating. *J. Atmos. Sci.*, **67**, 1779–1805, https://doi.org/10.1175/2010JAS3171.1.

Mueller, K. J., M. DeMaria, J. A. Knaff, J. P. Kossin, and T. H. Vonder Haar, 2006: Objective estimation of tropical cyclone wind structure from infrared satellite data. *Wea. Forecasting*, **21**, 990–1005, https://doi.org/10.1175/WAF955.1.

NCODA, 2019: Nov 18: Navy's Coupled Ocean Data Assimilation (NCODA) 3-d ocean data. Accessed 1 September 2020, ftp://usgodae.org/pub/outgoing/fnmoc/models/glb_ocn/.

Nguyen, L. T., R. F. Rogers, and P. D. Reasor, 2017: Thermodynamic and kinematic influences on precipitation symmetry in sheared tropical cyclones: Bertha and Cristobal (2014). *Mon. Wea. Rev.*, **145**, 4423–4446, https://doi.org/10.1175/MWR-D-17-0073.1.

——, ——, J. Zawislak, and J. A. Zhang, 2019: Assessing the influence of convective downdrafts and surface enthalpy fluxes on tropical cyclone intensity change in moderate

vertical wind shear. *Mon. Wea. Rev.*, **147**, 3519–3534, https://doi.org/10.1175/MWR-D-18-0461.1.

Nolan, D. S., and B. F. Farrell, 1999: The intensification of two-dimensional swirling flows by stochastic asymmetric forcing. *J. Atmos. Sci.*, **56**, 3937–3962, https://doi.org/10.1175/1520-0469(1999)056<3937:TIOTDS>2.0.CO;2.

——, and L. D. Grasso, 2003: Nonhydrostatic, three-dimensional perturbations to balanced, hurricane-like vortices. Part II: Symmetric response and nonlinear simulations. *J. Atmos. Sci.*, **60**, 2717–2745, https://doi.org/10.1175/1520-0469(2003)060<2717:NTPTBH>2.0.CO;2.

——, and M. G. McGauley, 2012: Tropical cyclogenesis in wind shear: Climatological relationships and physical processes. *Cyclones: Formation, Triggers, and Control*, K. Oouchi and H. Fudeyasu, Eds., Nova Science Publishers, 1–35.

——, Y. Moon, and D. P. Stern, 2007: Tropical cyclone in-tensification from asymmetric convection: Energetics and efficiency. *J. Atmos. Sci.*, **64**, 3377–3405, https://doi.org/10.1175/JAS3988.1.

Onderlinde, M. J., and D. S. Nolan, 2014: Environmental helicity and its effects on development and intensification of tropical cyclones. *J. Atmos. Sci.*, **71**, 4308–4320, https://doi.org/10.1175/JAS-D-14-0085.1.

——, and ——, 2016: Tropical cyclone–relative environmental helicity and the pathways to intensification in shear. *J. Atmos. Sci.*, **73**, 869–890, https://doi.org/10.1175/JAS-D-15-0261.1.

Pielke, R. A., Jr, and C. W. Landsea, 1998: Normalized hurricane damages in the United States: 1925–95. *Wea. Forecasting*, **13**, 621–631, https://doi.org/10.1175/1520-0434(1998)013<0621:NHDITU>2.0.CO;2.

——, J. Gratz, C. W. Landsea, D. Collins, M. A. Saunders, and R. Muslin, 2008: Normalized hurricane damage in the United States: 1900–2005. *Nat. Hazards Rev.*, **9**, 29–42, https://doi.org/10.1061/(ASCE)1527-6988(2008)9:1(29).

Rappin, E. D., and D. S. Nolan, 2012: The effect of vertical shear orientation on tropical cyclogenesis. *Quart. J. Roy. Meteor. Soc.*, **138**, 1035–1054, https://doi.org/10.1002/qj.977.

Reasor, P. D., R. F. Rogers, and S. Lorsolo, 2013: Environmental flow impacts on tropical cyclone structure diagnosed from airborne Doppler radar composites. *Mon. Wea. Rev.*, **141**, 2949–2969, https://doi.org/10.1175/MWR-D-12-00334.1.

Reynolds, R. W., and T. M. Smith, 1993: An improved real-time global sea surface temperature analysis. *J. Climate*, **6**, 114–119, https://doi.org/10.1175/1520-0442(1993)006<0114:AIRTGS>2.0.CO;2.

Riemer, M., 2016: Meso-β-scale environment for the stationary band complex of vertically sheared tropical cyclones. *Quart. J. Roy. Meteor. Soc.*, **142**, 2442–2451, https://doi.org/10.1002/qj.2837.

——, M. T. Montgomery, and M. E. Nicholls, 2010: A new paradigm for intensity modification of tropical cyclones: Thermodynamic impact of vertical wind shear on the inflow layer. *Atmos. Chem. Phys.*, **10**, 3163–3188, https://doi.org/10.5194/acp-10-3163-2010.

——, ——, and ——, 2013: Further examination of the thermodynamic modification of the inflow layer of tropical cyclones by vertical wind shear. *Atmos. Chem. Phys.*, **13**, 327–346, https://doi.org/10.5194/acp-13-327-2013.

Rios-Berrios, R., and R. D. Torn, 2017: Climatological analysis of tropical cyclone intensity changes under moderate vertical wind shear. *Mon. Wea. Rev.*, **145**, 1717–1738, https://doi.org/10.1175/MWR-D-16-0350.1.

——, ——, and C. A. Davis, 2016a: An ensemble approach to investigate tropical cyclone intensification in sheared environments. Part I: Katia (2011). *J. Atmos. Sci.*, **73**, 71–93, https://doi.org/10.1175/JAS-D-15-0052.1.

——, ——, and ——, 2016b: An ensemble approach to investigate tropical cyclone intensification in sheared environments. Part II: Ophelia (2011). *J. Atmos. Sci.*, **73**, 1555–1575, https://doi.org/10.1175/JAS-D-15-0245.1.

——, C. A. Davis, and R. D. Torn, 2018: A hypothesis for the intensification of tropical cyclones under moderate vertical wind shear. *J. Atmos. Sci.*, **75**, 4149–4173, https://doi.org/10.1175/JAS-D-18-0070.1.

Rogers, R., and Coauthors, 2006: The Intensity Forecasting Experiment: A NOAA multiyear field program for improving tropical cyclone intensity forecasts. *Bull. Amer. Meteor. Soc.*, **87**, 1523–1538, https://doi.org/10.1175/BAMS-87-11-1523.

——, S. Lorsolo, P. Reasor, J. Gamache, and F. Marks, 2012: Multiscale analysis of tropical cyclone kinematic structure from airborne Doppler radar composites. *Mon. Wea. Rev.*, **140**, 77–99, https://doi.org/10.1175/MWR-D-10-05075.1.

——, and Coauthors, 2013a: NOAA's hurricane intensity forecasting experiment: A progress report. *Bull. Amer. Meteor. Soc.*, **94**, 859–882, https://doi.org/10.1175/BAMS-D-12-00089.1.

——, P. D. Reasor, and S. Lorsolo, 2013b: Airborne Doppler observations of the inner-core structural differences between intensifying and steady-state tropical cyclones. *Mon. Wea. Rev.*, **141**, 2970–2991, https://doi.org/10.1175/MWR-D-12-00357.1.

——, ——, and J. Zhang, 2015: Multiscale structure and evolution of Hurricane Earl (2010) during rapid intensification. *Mon. Wea. Rev.*, **143**, 536–562, https://doi.org/10.1175/MWR-D-14-00175.1.

——, J. Zhang, J. Zawislak, H. Jiang, G. R. Alvey III, E. J. Zipser, and S. N. Stevenson, 2016: Observations of the structure and evolution of Hurricane Edouard (2014) during intensity change. Part II: Kinematic structure and the distribution of deep convection. *Mon. Wea. Rev.*, **144**, 3355–3376, https://doi.org/10.1175/MWR-D-16-0017.1.

——, P. D. Reasor, J. A. Zawislak, and L. T. Nguyen, 2020: Precipitation processes and vortex alignment during the intensification of a weak tropical cyclone in moderate vertical shear. *Mon. Wea. Rev.*, **148**, 1899–1929, https://doi.org/10.1175/MWR-D-19-0315.1.

Rudzin, J. E., S. Chen, E. R. Sanabia, and S. R. Jayne, 2020: The air-sea response during Hurricane Irma's (2017) rapid intensification over the Amazon-Orinoco River plume as measured by atmospheric and oceanic observations. *J. Geophys. Res. Atmos.*, **125**, e2019JD032368, https://doi.org/10.1029/2019JD032368.

Ryglicki, D. R., J. H. Cossuth, D. Hodyss, and J. D. Doyle, 2018: The unexpected rapid intensification of tropical cyclones in moderate vertical wind shear. Part I: Overview and observations. *Mon. Wea. Rev.*, **146**, 3773–3800, https://doi.org/10.1175/MWR-D-18-0020.1.

Saha, S., and Coauthors, 2010: The NCEP Climate Forecast System Reanalysis. *Bull. Amer. Meteor. Soc.*, **91**, 1015–1058, https://doi.org/10.1175/2010BAMS3001.1.

Shay, L. K., G. J. Goni, and P. G. Black, 2000: Effects of a warm oceanic feature on Hurricane Opal. *Mon. Wea. Rev.*, **128**, 1366–1383, https://doi.org/10.1175/1520-0493(2000)128<1366:EOAWOF>2.0.CO;2.

Stern, D. P., and D. S. Nolan, 2009: Reexamining the vertical structure of tangential winds in tropical cyclones: Observations and theory. *J. Atmos. Sci.*, **66**, 3579–3600, https://doi.org/10.1175/2009JAS2916.1.

Stevenson, S. N., K. L. Corbosiero, and J. Molinari, 2014: The convective evolution and rapid intensification of Hurricane Earl (2010). *Mon. Wea. Rev.*, **142**, 4364–4380, https://doi.org/10.1175/MWR-D-14-00078.1.

——, ——, M. DeMaria, and J. L. Vigh, 2018: A 10-year survey of tropical cyclone inner-core lightning bursts and their relationship to intensity change. *Wea. Forecasting*, **33**, 23–36, https://doi.org/10.1175/WAF-D-17-0096.1.

Tang, B., and K. Emanuel, 2010: Midlevel ventilation's constraint on tropical cyclone intensity. *J. Atmos. Sci.*, **67**, 1817–1830, https://doi.org/10.1175/2010JAS3318.1.

——, and ——, 2012: Sensitivity of tropical cyclone intensity to ventilation in an axisymmetric model. *J. Atmos. Sci.*, **69**, 2394–2413, https://doi.org/10.1175/JAS-D-11-0232.1.

Tao, C., and H. Jiang, 2015: Distributions of shallow to very deep precipitation–convection in rapidly intensifying tropical cyclones. *J. Climate*, **28**, 8791–8824, https://doi.org/10.1175/JCLI-D-14-00448.1.

——, ——, and J. Zawislak, 2017: The relative importance of stratiform and convective rainfall in rapidly intensifying tropical cyclones. *Mon. Wea. Rev.*, **145**, 795–809, https://doi.org/10.1175/MWR-D-16-0316.1.

Tuleya, R. E., and Y. Kurihara, 1981: A numerical study on the effects of environmental flow on tropical storm genesis. *Mon. Wea. Rev.*, **109**, 2487–2506, https://doi.org/10.1175/1520-0493(1981)109<2487:ANSOTE>2.0.CO;2.

Uhlhorn, E. W., P. G. Black, J. L. Franklin, M. Goodberlet, J. Carswell, and A. S. Goldstein, 2007: Hurricane surface wind measurements from an operational stepped frequency microwave radiometer. *Mon. Wea. Rev.*, **135**, 3070–3085, https://doi.org/10.1175/MWR3454.1.

Velden, C. S., and J. Sears, 2014: Computing deep-tropospheric vertical wind shear analyses for tropical cyclone applications: Does the methodology matter? *Wea. Forecasting*, **29**, 1169–1180, https://doi.org/10.1175/WAF-D-13-00147.1.

Wadler, J. B., R. F. Rogers, and P. D. Reasor, 2018a: The relationship between spatial variations in the structure of convective bursts and tropical cyclone intensification as determined by airborne Doppler radar. *Mon. Wea. Rev.*, **146**, 761–780, https://doi.org/10.1175/MWR-D-17-0213.1.

——, J. A. Zhang, B. Jaimes, and L. K. Shay, 2018b: Downdrafts and the evolution of boundary layer thermodynamics in Hurricane Earl (2010) before and during rapid intensification. *Mon. Wea. Rev.*, **146**, 3545–3565, https://doi.org/10.1175/MWR-D-18-0090.1.

——, ——, ——, and ——, 2021a: The rapid intensification of Hurricane Michael (2018): Storm structure and the relationship to environmental and air–sea interactions. *Mon. Wea. Rev.*, **149**, 245–267, https://doi.org/10.1175/MWR-D-20-0145.1.

——, D. S. Nolan, J. A. Zhang, and L. K. Shay, 2021b: The thermodynamic characteristics of downdrafts in tropical cyclones using idealized simulations of different intensities. *J. Atmos. Sci.*, **78**, 3503–3524, https://doi.org/10.1175/JAS-D-21-0006.1.

Wang, Y., 2009: How do outer spiral rainbands affect tropical cyclone structure and intensity. *J. Atmos. Sci.*, **66**, 1250–1273, https://doi.org/10.1175/2008JAS2737.1.

Willoughby, H. E., and M. B. Chelmow, 1982: Objective determination of hurricane tracks from aircraft observations. *Mon. Wea. Rev.*, **110**, 1298–1305, https://doi.org/10.1175/1520-0493(1982)110<1298:ODOHTF>2.0.CO;2.

——, F. D. Marks Jr., and R. J. Feinberg, 1984: Stationary and moving convective bands in hurricanes. *J. Atmos. Sci.*, **41**, 3189–3211, https://doi.org/10.1175/1520-0469(1984)041<3189:SAMCBI>2.0.CO;2.

Zagrodnik, J. P., and H. Jiang, 2014: Rainfall, convection, and latent heating distributions in rapidly intensifying tropical cyclones. *J. Atmos. Sci.*, **71**, 2789–2809, https://doi.org/10.1175/JAS-D-13-0314.1.

Zawislak, J., H. Jiang, G. R. Alvey III, E. J. Zipser, R. F. Rogers, J. A. Zhang, and S. N. Stevenson, 2016: Observations of the structure and evolution of Hurricane Edouard (2014) during intensity change. Part I: Relationship between the thermodynamic structure and precipitation. *Mon. Wea. Rev.*, **144**, 3333–3354, https://doi.org/10.1175/MWR-D-16-0018.1.

Zhang, J. A., and R. F. Rogers, 2019: Effects of parameterized boundary layer structure on hurricane rapid intensification in shear. *Mon. Wea. Rev.*, **147**, 853–871, https://doi.org/10.1175/MWR-D-18-0010.1.

——, P. G. Black, J. R. French, and W. M. Drennan, 2008: First direct measurements of enthalpy flux in the hurricane boundary layer: The CBLAST results. *Geophys. Res. Lett.*, **35**, L14813, https://doi.org/10.1029/2008GL034374.

——, R. Rogers, P. Reasor, E. Uhlhorn, and F. Marks, 2013: Asymmetric hurricane boundary layer structure from dropsonde composites in relation to the environmental vertical wind shear. *Mon. Wea. Rev.*, **141**, 3968–3984, https://doi.org/10.1175/MWR-D-12-00335.1.

——, J. J. Cione, E. A. Kalina, E. W. Uhlhorn, T. Hock, and J. A. Smith, 2017: Observations of infrared sea surface temperature and air-sea interaction in Hurricane Edouard (2014) using GPS dropsondes. *J. Atmos. Oceanic Technol.*, **34**, 1333–1349, https://doi.org/10.1175/JTECH-D-16-0211.1.

——, J. P. Dunion, and D. S. Nolan, 2020: In situ observations of the diurnal variation in the boundary layer of mature hurricanes. *Geophys. Res. Lett.*, **47**, 2019GL086206, https://doi.org/10.1029/2019GL086206.